Trapping and transport of inertial particles in a Taylor-Green vortex: Effects of added mass and history force

Prabhash Kumar, Anu V. S. Nath, Mahesh Panchagnula, and Anubhab Roy*
Department of Applied Mechanics & Biomedical Engineering, Indian Institute of Technology Madras, Chennai 600036, India

(Received 10 March 2025; accepted 10 September 2025; published 23 October 2025)

We investigate the dynamics of *small* inertial particles in a two-dimensional, steady Taylor-Green vortex flow. A classic study by Taylor (1940) showed that infinitely heavy inertial point particles (having density parameter $R = 1$) are trapped by the flow separatrices when the particle Stokes number St, which measures the particle's inertia, is less than $1/4$. Here, we consider finitely heavy particles, incorporating the previously neglected effects of added mass and the Boussinesq-Basset history force. Using linear stability analysis near fixed points, we determine the critical parametric conditions in the St-R plane that lead to particle trapping within vortex cells. Including the added mass effect identifies additional fixed points beyond the traditional ones located at the vortex cell corners, and we analyze their stability. Numerical analysis of the full nonlinear system confirms the existence of distinct particle behaviors—trapped, diffusive, and ballistic—depending on initial conditions, consistent with Nath *et al.* [Phys. Rev. Fluids **9**, 014302 (2024)], with modifications due to added mass effect. We delineate the regions in the St-R plane where these behaviors dominate based on the prominent particle dynamics. However, when both the history force and added mass effect are included, all particles exhibit ballistic motion regardless of St and R.

DOI: 10.1103/jv92-2mx3

I. INTRODUCTION

The transport and dispersion of *small* inertial particles in fluid flow play a crucial role in numerous physiological, environmental, and engineering applications. Examples include particulate transport in pulmonary airways [1], blood flow in arteries [2], the dynamics of water droplets in turbulent atmospheric clouds [3], and the movement of dust and debris in hurricanes [4]. Additionally, inertial particle transport is fundamental to various industrial processes such as spray drying, pollution control, and slurry transport, among others [5].

Maxey and Riley [6] derived an equation of motion to describe the dynamics of a small, rigid sphere in a nonuniform flow as

$$m_p \frac{d\mathbf{v}}{dt} = m_f \frac{D\mathbf{u}}{Dt} + \frac{m_f}{2}\left(\frac{D\mathbf{u}}{Dt} - \frac{d\mathbf{v}}{dt}\right) - 6\pi\,\mu\,a\,(\mathbf{v}-\mathbf{u}) - 6a^2\,\rho_f\,\sqrt{\pi\,\nu}\left[\int_{t_0}^{t}\left(\frac{d\mathbf{v}}{dt'} - \frac{d\mathbf{u}}{dt'}\right)\frac{dt'}{\sqrt{t-t'}} + \frac{\mathbf{v}_0-\mathbf{u}_0}{\sqrt{t-t_0}}\right], \tag{1}$$

where m_p and m_f are the particle mass and the mass of the displaced fluid, respectively. The densities of the particle and fluid are denoted by ρ_p and ρ_f, respectively. The particle's Lagrangian velocity is

*Contact author: anubhab@iitm.ac.in

represented by $\mathbf{v}$, while $\mathbf{u}$ is the fluid velocity sampled at the particle's position $\mathbf{x}$, where $d\mathbf{x}/dt = \mathbf{v}$. The particle has a radius a, and the fluid properties are characterized by the dynamic viscosity μ and the kinematic viscosity $\nu = \mu/\rho_f$. The initial time is denoted by t_0, with the corresponding initial velocities of the particle and fluid given by $\mathbf{v}(t = t_0) = \mathbf{v}_0$ and $\mathbf{u}(t = t_0) = \mathbf{u}_0$, respectively. The material derivative $D\mathbf{u}/Dt = \partial\mathbf{u}/\partial t + \mathbf{u}\cdot\nabla\,\mathbf{u}$ represents the fluid acceleration. The first two terms on the right-hand side of equation (1) correspond to inertial forces, which include the pressure gradient force and the added mass effect. The remaining two terms are viscous forces, comprising Stokes drag and the Boussinesq-Basset history force (or simply "history force"). In its original form, equation (1) includes Faxén correction terms as well, which are neglected here as they become insignificant for particles significantly smaller than the flow length scale [7,8]. We also neglect the gravitational settling effects in the current analysis. The presence of the history force makes the Maxey-Riley equation an integrodifferential equation, rendering its analytical solution highly nontrivial. Additionally, numerical solutions are computationally expensive and require significant memory resources [9,10]. To avoid these challenges, two simplified models of the Maxey-Riley equation are widely adopted in the literature. One of these models is given (in nondimensional form) as

$$\frac{d\mathbf{v}}{dt} = -\frac{1}{\mathrm{St}}(\mathbf{v} - \mathbf{u}), \tag{2}$$

which applies in the limit of infinitely heavy particles, where the particle-to-fluid density ratio is very large ($\rho_p/\rho_f \gg 1$) [8]. The Stokes number, denoted as St in equation (2), is a dimensionless measure of a particle's inertia, defined as the ratio of the particle relaxation time $\tau_p = m_p/(6\pi\mu a)$ to the relevant flow timescale. The relaxation time τ_p characterizes the timescale over which a particle adjusts its velocity to match the surrounding flow velocity. The model in Eq. (2) is commonly used to study the transport of particles and droplets in various atmospheric turbulent flows [8,11–14]. The other model is a reduced-order Maxey-Riley equation, derived by Ferry and Balachandar [15] building on earlier work by Maxey [16] and Druzhinin [17], also known as the inertial equation [18], given by

$$\mathbf{v} = \mathbf{u} + \mathrm{St}\left(\frac{2 - 3R}{R}\right)\frac{D\mathbf{u}}{Dt} + \mathcal{O}(\mathrm{St}^{3/2}), \tag{3}$$

where $R = 2\rho_p/(2\rho_p + \rho_f)$ is the density parameter, $R = 1$ corresponds to the infinitely heavy particle limit ($\rho_p \gg \rho_f$), $R = 0$ corresponds to very light particles ($\rho_p \ll \rho_f$), and $R = 2/3$ corresponds to density-matched particles ($\rho_p = \rho_f$). The inertial equation is valid in the limit $\mathrm{St} \ll R$, implying that the particle velocity closely follows the flow velocity with an inertial correction from fluid acceleration. This equation is derived through asymptotic analysis under the condition $\mathrm{St} \ll R$, where the influence of Stokes drag and inertial forces occur at $\mathcal{O}(\mathrm{St})$ while the influence of the history force appears only at higher-order terms. The original derivation by Ferry and Balachandar [15] suggested that the next correction term would be of the order $\mathcal{O}(\mathrm{St}^{3/2})$ when accounting for the history force. However, in the absence of the history force, the correction terms are weaker, of the order $\mathcal{O}(\mathrm{St}^2)$ [16–18].

The transport of inertial particles in cellular flows, such as the Taylor-Green (TG) vortex, has been extensively investigated using various forms of the Maxey-Riley equation. One of the earliest works by Maxey [7] demonstrated that particle inertia and density contrast critically determine the spatial distribution of inertial particles in both cellular flows. The study showed that inertial particles deviate from fluid streamlines, with heavy particles preferentially accumulating in high-strain regions, such as the corners of cellular flows, and lighter particles clustering near vortex centers. This asymmetry enables heavy particles to cross the flow separatrices and adopt nonuniform distributions. Building on these insights, Crisanti *et al.* [19] and Crisanti *et al.* [20] investigated particle transport in steady TG vortex flows, identifying that lighter particles migrate toward vortex centers while heavier particles follow chaotic trajectories, resulting in inertial diffusion. Wang *et al.* [21] further established that chaotic particle motion strongly depends on Stokes number (St) and

density parameter R, with chaotic dispersion rates inversely related to mixing efficiency. Raju and Meiburg [22] analyzed particle dynamics in vortical and extensional flows, finding that optimal ejection and entrapment occur at intermediate Stokes numbers, with particle-to-fluid density ratio and gravity playing significant roles. More recently, Nath *et al.* [23] and Nath *et al.* [24] explored infinitely heavy particle dynamics in TG vortex flows, confirming classical trapping thresholds [25] and identifying nonergodic behavior, where particles may exhibit trapped, diffusive, or ballistic dispersion depending on initial conditions. These studies also drew analogies to soft Lorentz gas systems [26], highlighting the irregular and sometimes discontinuous dispersion variation with the Stokes number. It has even been shown by Nath and Roy [27] that infinitely heavy particles in an isolated vortex, when slightly perturbed by interactions with nearby vortices, can undergo chaotic transport. Dagan [28] derived analytical solutions for the dispersion of infinitely heavy inertial particles in the TG vortex flow. In the limit $\mathrm{St} \ll 1$, the authors simplified the governing equations and obtained explicit mathematical expressions, which provide analytical insights into particle trajectories and velocities. Despite these advances, most prior works have neglected the history force due to its mathematical complexity. However, several studies have highlighted its importance: Lasheras and Tio [29] showed that the history force appears as a higher-order term for small Stokes numbers, while Druzhinin and Ostrovsky [30] and Candelier *et al.* [31] demonstrated that it can significantly alter particle trajectories, particularly in separatrix crossing and ejection from vortex centers. In turbulent flows, Daitche [32] found that the history force reduces particle clustering by making particles behave more like tracers, though this effect diminishes for infinitely heavy particles ($R \sim 1$). Collectively, these studies illustrate the roles of particle inertia, density ratio, and hydrodynamic forces in governing particle transport in cellular flows and motivate an investigation into the role of the history force in such systems.

This study investigates the dynamics of inertial particles in the TG vortex by modeling their motion using Eq. (1). The primary objective is to explore the behavior of heavy particles over a broader range of particle-fluid density ratios and to examine the influence of inertial forces and the often-neglected history force on their dynamics. This article is structured as follows: In Sec. II, we discuss the flow field, outline our objectives, and list the assumptions we made while also examining the nondimensional form of the equations of motion along with relevant nondimensional numbers. Before we dive into the analysis of particle dynamics in the TG vortex, we first explore their behavior near fixed points—the fundamental components of the TG vortex—using linear stability analysis in Sec. III by linearizing the full equation of motion around the fixed points of the TG vortex to investigate the leading-order dynamics. Furthermore, this section will address the emergence of additional fixed points induced by inertial forces. In Sec. IV, we conduct a numerical analysis to study particle dynamics within the fully nonlinear TG vortex flow in the absence of history force and analyze the effects of history force on the dynamics in Sec. V. Finally, we highlight the key findings and provide concluding remarks in Sec. VI.

II. PROBLEM FORMULATION

The TG vortex represents a 2D, steady, laminar, and incompressible flow field characterized by the stream function

$$\psi^*(x^*,\ y^*) = U\,L\,\sin\left(\frac{x^*}{L}\right)\,\sin\left(\frac{y^*}{L}\right). \tag{4}$$

Here, $(\,)^*$ denotes dimensional quantities. The TG flows feature doubly periodic arrays of cells comprising four counter-rotating vortices of cell size L, arranged in an unbounded 2D space. The points where the flow velocity vanishes are known as fixed points. For the TG vortex we have considered, these fixed points are located at the vortex centers $(n\pi + \pi/2, m\pi + \pi/2)$, and at the corners of the vortex cells $(n\pi, m\pi)$ for integers n and m. Each vortex cell features fixed points at its corners and center, while each cell boundary connecting the corner fixed points is a flow separatrice. For example, $n = m = 0$ describes a center fixed point at $(\pi/2,\ \pi/2)$, and a corner

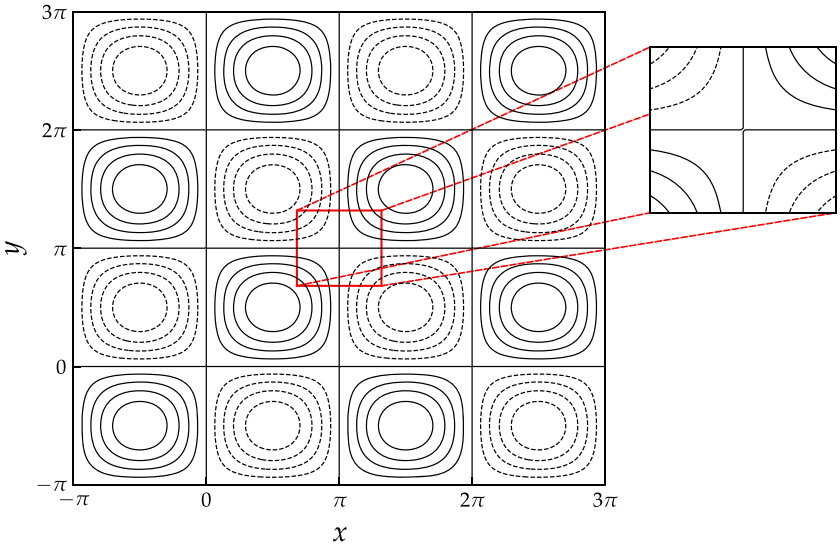

FIG. 1. The TG vortex flow displays streamlines. The inset provides a zoomed-in view of the flow patterns near a stagnant point at $(\pi,\ \pi)$. Solid contour lines indicate anti-clockwise rotation, while dashed contour lines represent clockwise rotation.

fixed point at the origin (0, 0). The maximum velocity, U, occurs along the boundaries of the vortices. Additionally, the flow exhibits mirror symmetry and periodic repetition in both the x and y directions. Inside every cell, fluid elements orbit along the streamlines with regular periodic motion. The period of this motion depends on the initial positions of the fluid elements: it is $2\pi\ L/U$ near the vortex center and becomes infinite near the cell boundaries. We use the characteristic flow length scale L and velocity scale U to nondimensionalize the system. The velocity components for the TG vortex are thus given in nondimensional form as $u_x = \sin x\ \cos y$ and $u_y = -\cos x\ \sin y$. Here, variables without $(\,)^*$ represent nondimensional quantities. In Fig. 1, we illustrate the streamlines of TG flow in the $[-\pi, 3\pi] \times [-\pi, 3\pi]$ nondimensional space. Fluid parcels traverse along the flow separatrices as they approach the corner fixed points. At the same time, heavy inertial particles ($\rho_p > \rho_f$ and $\mathrm{St} > 0$) may cross these separatrices/cell boundaries depending on some parametric conditions, as we will see later.

The objective of this study is to investigate the dynamics of heavy ($\rho_p > \rho_f$) inertial particles in the TG vortex flow described by Eq. (4). We model the inertial particles as *small*, rigid spheres with a radius $a \ll L$, and we assume that the particle suspension is dilute enough so that particles do not interact with one another and the feedback effect from the particles to the fluid is minimal. This allows us to treat the system as one-way coupled. Under this assumption, we can utilize the Maxey-Riley equation [Eq. (1)] to model the particle motion. After rearranging the terms in Eq. (1) and substituting the velocity field from Eq. (4), along with scaling by the characteristic flow scales U and L, the governing equations for particle dynamics can be expressed in a nondimensional, component form as

$$\frac{dv_x}{dt} = -\frac{R}{\mathrm{St}}\left(v_x - \sin x\ \cos y\right) + 3\left(1-R\right)\ \sin x\ \cos x - \frac{\kappa}{\sqrt{\pi}}\left[\frac{v_{x_0} - \sin x_0 \cos y_0}{\sqrt{t}} + \int_0^t \frac{1}{\sqrt{t-t'}}\left(\frac{dv_x}{dt'} - v_x \cos x \cos y + v_y \sin x \sin y\right)dt'\right], \tag{5a}$$

$$\frac{dv_y}{dt} = -\frac{R}{\mathrm{St}}\left(v_y + \sin y\,\cos x\right) + 3\left(1-R\right)\,\sin y\,\cos y - \frac{\kappa}{\sqrt{\pi}}\left[\frac{v_{y_0} + \cos x_0 \sin y_0}{\sqrt{t}} + \int_0^t \frac{1}{\sqrt{t-t'}}\left(\frac{dv_y}{dt'} - v_x \sin x \sin y + v_y \cos x \cos y\right)dt'\right], \tag{5b}$$

with $v_x = dx/dt$ and $v_y = dy/dt$. Here, the initial time is set to zero, i.e., $t_0 = 0$, and the corresponding variables are notated as x_0, y_0, v_{x_0} and v_{y_0}. In these equations, the variables x and y represent the particle positions, while v_x and v_y denote their velocities. Together, these four variables constitute the dynamical state of the system in a four-dimensional (4D) phase space. The governing system involves two independent nondimensional parameters: the density parameter R and the Stokes number St. As previously noted, the Stokes number St characterizes particle inertia, where $\mathrm{St} = 0$ corresponds to inertialess particles that perfectly trace the fluid streamlines. The density parameter R quantifies the relative density of particles with respect to the fluid. Specifically, $R = 1$ corresponds to infinitely heavy particles ($\rho_p \gg \rho_f$), while $R = 2/3$ represents density-matched particles particles ($\rho_p = \rho_f$). In contrast, $R = 0$ characterizes very light particles, such as bubbles ($\rho_p \ll \rho_f$). The coefficient of the history force, κ, is related to the other parameters as

$$\kappa = 3\sqrt{\frac{(1-R)}{R}\,\frac{1}{\mathrm{St}}}. \tag{6}$$

Note that our definition of the Stokes number, St, differs from that used in other studies [9,10,33]. These studies formulate St using the timescale a^2/ν, representing the timescale over which momentum diffuses in the fluid. In contrast, our definition expresses the particle response time τ_p, which is $(2\rho_p/9\rho_f)a^2/\nu$, characterizing how quickly the particle's momentum adjusts to the surrounding fluid streamlines. For our analysis, we focus on the regime $2/3 < R < 1$ and $0.1 < \mathrm{St} < 1.0$, concentrating on the dynamics of particles that are finitely heavier than the fluid and emphasizing investigating the role of inertial and history forces on their transport features.

The governing system of Eqs. (5) consists of coupled nonlinear integrodifferential equations, making analytical treatment highly challenging. Consequently, we resort to numerical methods to solve for particle dynamics. However, before proceeding with numerical calculations, we predict the particle behavior analytically by simplifying the flow field. Note that the nonlinearity of the system originates from the nonlinear nature of the TG vortex flow, which contains key flow structures such as fixed points of type vortex centers and stagnation regions. We study particle motion near these structures by linearizing the flow in their vicinity to gain analytical insights. Of particular interest are the stagnation regions, as previous studies [19,21] have shown that particles in a TG vortex flow primarily migrate between vortex cells through the regions surrounding these points. Specifically, infinitely heavy inertial particles ($R = 1$) have been found to escape vortex cells near stagnation regions if their Stokes number exceeds a critical threshold of $\mathrm{St} = 1/4$ [23,34]. In the following sections, we analyze how the inclusion of inertial forces and the history force modifies particle leakage near stagnation regions. We begin by discussing the dynamics of particles near fixed points, using linearized flow approximations to extract analytical results. Subsequently, we examine how the inherent nonlinearity of the TG flow influences particle transport and longtime dispersion.

III. PARTICLE DYNAMICS NEAR FIXED POINTS

Before analyzing the full nonlinear system of the TG flow, we first examine particle dynamics near the fixed points analytically. Initially, we only consider the effects of Stokes drag and inertial forces, neglecting the history force. We then incorporate the history force to evaluate its impact on particle transport behavior. The equations of motion for an inertial particle in the TG vortex flow, in

the absence of the history force, can be derived from Eq. (5) by omitting the terms multiplying by κ, as

$$\dot{x} = v_x, \quad \dot{v}_x = -\frac{R}{\mathrm{St}}\,(v_x - \sin x\,\cos y) + 3\,(1-R)\,\sin x\,\cos x, \tag{7a}$$

$$\dot{y} = v_y, \quad \dot{v}_y = -\frac{R}{\mathrm{St}}\,(v_y + \sin y\,\cos x) + 3\,(1-R)\,\sin y\,\cos y. \tag{7b}$$

These equations are coupled and nonlinear but remain ordinary differential equations. They can be rewritten by defining a modified effective flow field that incorporates the modifications introduced by the fluid inertia term, allowing it to be absorbed into the Stokes drag as

$$\dot{x} = v_x, \quad \dot{v}_x = -\frac{1}{\mathrm{St_m}}\,(v_x - u_{xe}), \tag{8a}$$

$$\dot{y} = v_y, \quad \dot{v}_y = -\frac{1}{\mathrm{St_m}}\,(v_y - u_{ye}), \tag{8b}$$

where the modified effective flow field is defined as

$$u_{xe} = \sin x\,(\cos y + \gamma^{-1}\cos x), \quad u_{ye} = \sin y\,(-\cos x + \gamma^{-1}\cos y). \tag{9}$$

The relevant dimensionless parameters are defined as

$$\mathrm{St}_m = \frac{\mathrm{St}}{R}, \quad \mathrm{St}_{c_p} = \frac{R}{3(1-R)}, \quad \gamma = \frac{\mathrm{St}_{c_p}}{\mathrm{St}}. \tag{10}$$

The significance of this critical Stokes number, St_{c_p}, will become evident later. The modified flow field differs significantly from the conventional TG vortex flow due to its dependence on St and R, meaning that different particles, depending on their size and density, can experience different effective flow fields. Interestingly, the modified flow field $\mathbf{u}_e = [u_{xe}, u_{ye}]^T$ is compressible, with a nonzero divergence given by $\nabla \cdot \mathbf{u}_e = \gamma^{-1}(\cos 2x + \cos 2y)$. Notice the similarity of Eqs. (8) and (2); i.e., in the absence of history force, the motion of inertial particles with Stokes number St and a finite density ratio R in a flow $\mathbf{u}$ is equivalent to the motion of infinitely heavy particles with an effective Stokes number $\mathrm{St_m}$ in a modified flow $\mathbf{u}_e$. In the infinitely heavy particle limit ($R \to 1$), the modified flow field becomes the usual TG vortex flow, $\mathrm{St_m}$ reduces to St, and the modified equations of motion [Eqs. (8a) and (8b)] simplify to the simplified Maxey–Riley equation [Eq. (2)] for TG vortex flow. The same idea applies to any general flow field $\mathbf{u}$, for which a corresponding modified flow field can be defined as

$$\mathbf{u}_e = \mathbf{u} + \gamma^{-1}\,\frac{D\mathbf{u}}{Dt}. \tag{11}$$

It is important to distinguish between the effective flow field defined in Eq. (11) and the reduced particle velocity field given in Eq. (3). Although both are written in terms of the flow velocity $\mathbf{u}$ and its material derivative $D\mathbf{u}/Dt$, they differ in the values of their coefficients and, more importantly, in what they represent. The effective flow field in Eq. (11) describes a modified version of the fluid flow, while Eq. (3) approximates the velocity of an inertial particle. This reduced particle velocity is a valid approximation only when the Stokes number is much smaller than the density ratio, i.e., $\mathrm{St} \ll R$. In contrast, the effective flow field in equation (11) provides an exact formulation that remains valid for any finite values of St and R. Furthermore, if we expand the particle velocity Eqs. (8) in the limit $\mathrm{St_m} \ll 1$ using the method of Ferry and Balachandar [15] (which corresponds to Eq. (3) with $R = 1$ and $\mathrm{St} = \mathrm{St_m}$), then we obtain $\mathbf{v} = \mathbf{u}_e - \mathrm{St_m}\,D\mathbf{u}_e/Dt + \mathcal{O}(\mathrm{St_m^{3/2}})$. Substituting $\mathbf{u}_e$ from Eq. (11) into this expansion recovers the expression in Eq. (3), as given by Ferry and Balachandar [15], which is valid for arbitrary values of R.

By setting $\dot{x} = 0$, $\dot{y} = 0$, $\dot{v}_x = 0$, and $\dot{v}_y = 0$ in Eqs. (7) or (8), we determine the fixed points of particles in this effective flow field. Here, trivially the solution gives $v_x = v_y = 0$. Apart from the fixed points located at the centers of the flow cells $(x,\ y) = (n\pi + \pi/2,\ m\pi + \pi/2)$ and at the

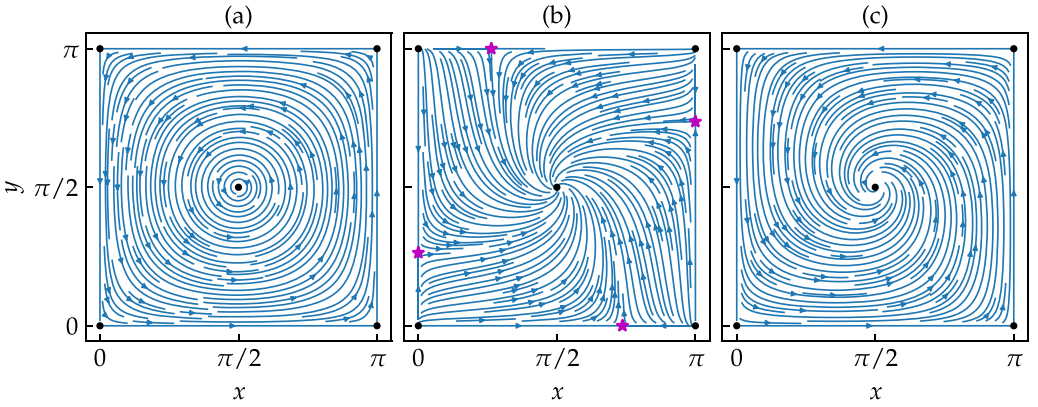

FIG. 2. (a) Locations of corner and center fixed points and the typical streamline pattern within a representative vortex cell of the Taylor–Green vortex flow. (b), (c) Flow pattern and fixed points of the effective velocity field $\mathbf{u}_e$ (corresponding to TG vortex), shown for different parameter combinations: (b) $R = 0.67$ and $\mathrm{St} = 1.0$; (c) $R = 0.67$ and $\mathrm{St} = 0.3$. Dot markers indicate the corner or center fixed points, while star markers indicate edge fixed points. Note that in panel (c), the edge fixed points are absent because $\mathrm{St} < \mathrm{St}_{c_p}$.

corners $(x,\ y) = (n\pi,\ m\pi)$—which, as noted earlier [see Figs. 1 or 2(a)], coincide with the fixed points of the flow—we also find additional fixed points. These new points lie on the flow separatrices and are located at $(x,\ y) = (n\pi,\ \cos^{-1}[(-1)^n \gamma])$ and $(\cos^{-1}[(-1)^{m+1}\gamma],\ m\pi)$, for any integers n and m. Since these additional fixed points appear along the separatrices or the boundaries between flow cells, we refer to them as edge fixed points (EFPs), and the fixed points at the cell corners are termed corner fixed points (CFPs) for distinguishing. For instance, in the basic vortex cell bounded by the separatrices at $x = 0$, $x = \pi$, $y = 0$ and $y = \pi$, four additional fixed points appear apart from the vortex center and the four CFPs, as shown in Fig. 2(b). These EFPs are located at $(0,\ \cos^{-1}[\gamma])$, $(\pi,\ \cos^{-1}[-\gamma])$, $(\cos^{-1}[\gamma],\ \pi)$, and $(\cos^{-1}[-\gamma],\ 0)$. Notably, these additional fixed points fall on the flow separatrices, but their exact location depends on γ, meaning their locations vary based on particle size and density. The existence of these fixed points is restricted to cases where $\gamma < 1$, which corresponds to $\mathrm{St} > \mathrm{St}_{c_p}$; for e.g., as shown in Fig. 2(c), the EFPs disappear when $\mathrm{St} = 0.3 < \mathrm{St}_{c_p}$ at $R = 0.67$. In Figs. 2(b) and 2(c), we show the streamline patterns of the effective flow field to depict the emergence and disappearance of EFPs visually. It is important to note that these streamline patterns do not convey the actual behavior of particles in the flow field. Also note that we have selected a $R = 0.67$ for this illustration as EFPs appear at lower values of St for this specific R while maintaining conditions relevant to moderately heavy particle scenarios. In the infinitely heavy particle limit ($R \to 1$), where $\mathrm{St}_{c_p} \to \infty$, no particle with a finite Stokes number would experience these EFPs. However, for any finite density ratio ($R < 1$), there exists a critical Stokes number St_{c_p} beyond which these additional fixed points emerge. Kinematically, EFPs, when they exist, behave like saddles. CFPs, however, behave as saddles before the EFPs appear, but transition to sources once the EFPs emerge, as explained in Appendix A.

In the following sections, we study the dynamics of inertial particles near a typical CFP and EFP by linearizing Eqs. (7) around those points. For the fixed point at the center of the cell, the surrounding flow behaves like solid-body rotation, where the velocity components are approximately $u_x \simeq -y$ and $u_y \simeq x$. Candelier *et al.* [31] used experiments and simulations to examine the dynamics of inertial particles in such a flow. They showed that even with the history force included, moderately heavy particles ($R > 2/3$) tend to get centrifuged out of the vortex center, while lighter particles ($R < 2/3$) tend to get trapped there, consistent with the prediction by Ref. [16]. Even though, for completeness, We have also included the detailed linear stability analysis of inertial particles near a typical vortex center in the absence of history force and further analyzed the

significance of history on their dynamics in Appendix B. The results show that in the absence of the history force, the vortex center behaves like a "2-spiral source" when $R > 2/3$, and like a "2-spiral sink" when $R < 2/3$, leading respectively to the centrifuging or accumulation of particles at the vortex center. While the qualitative nature of these fixed points remains unchanged upon including the history force, its presence reduces the migration rate of particles in both scenarios.

A. Particle dynamics near a corner fixed point of the TG vortex flow—Without history force

Each CFP in the TG vortex flow lies at the intersection of four neighboring vortices, as shown in Fig. 1. The flow near these points resembles a linear extensional flow, as illustrated in the inset of Fig. 1. For example, near the origin, the leading-order approximation of the velocity field gives $u_x \approx x$ and $u_y \approx -y$, indicating that the flow stretches along the x axis (extensional) and compresses along the y axis (compressional). Although this form approximates the velocity field near the fixed point at the origin, the same form applies near any CFP in the TG vortex flow, provided we adjust for the location and identify the correct stretching and compressing directions. Without loss of generality, focusing on the CFP at the origin, and ignoring the history force, the governing equation [Eq. (5)] simplifies to

$$\frac{1}{R}\ddot{x} + \frac{1}{\mathrm{St}}\dot{x} - x\left(\frac{3(1-R)}{R} + \frac{1}{\mathrm{St}}\right) = 0, \tag{12a}$$

$$\frac{1}{R}\ddot{y} + \frac{1}{\mathrm{St}}\dot{y} - y\left(\frac{3(1-R)}{R} - \frac{1}{\mathrm{St}}\right) = 0. \tag{12b}$$

Here $\dot{(\,)}$ represents time derivative d/dt. Since the Eqs. (12a) and (12b) form a set of two decoupled dynamical systems, the solution for the extensional (x) and compressional (y) directions can be determined separately as

$$x = C_1\, e^{\lambda_e^+ t} + C_2\, e^{\lambda_e^- t}, \quad \text{with } \lambda_e^{\pm} = \frac{1}{2}\left(-\frac{R}{\mathrm{St}} \pm \sqrt{\left(\frac{R}{\mathrm{St}}\right)^2 + 4\frac{R}{\mathrm{St}} + 12(1-R)}\right), \tag{13a}$$

$$y = C_3\, e^{\lambda_c^+ t} + C_4\, e^{\lambda_c^- t}, \quad \text{with } \lambda_c^{\pm} = \frac{1}{2}\left(-\frac{R}{\mathrm{St}} \pm \sqrt{\left(\frac{R}{\mathrm{St}}\right)^2 - 4\frac{R}{\mathrm{St}} + 12(1-R)}\right), \tag{13b}$$

The constants C_1, C_2, C_3, and C_4 are integration constants and depend on the initial conditions [see Eq. (C1)]. Here $\lambda_e^{\pm}$ and $\lambda_c^{\pm}$ are the eigenvalues of the system of Eqs. (12) when treated as a linear dynamical system. The colormap in Fig. 3 visualizes the real and imaginary parts of these eigenvalues across the St-R parametric plane. The nature of particle trajectories can be inferred from the eigenvalue set $(\lambda_e^+, \lambda_e^-, \lambda_c^+, \lambda_c^-)$, particularly from their signature. It is evident that eigenvalues $\lambda_e^{\pm}$ are always real since the discriminant $\mathfrak{D}_1 = (R/\mathrm{St})^2 + 4(R/\mathrm{St}) + 12(1-R)$ remains positive for all physically relevant values of $R < 1$. Consequently, λ_e^+ is always a positive real number, while λ_e^- is always negative, as shown in Figs. 3(a), 3(b), 3(e), and 3(f). The solution form in equation (13a) thus indicates that particles will move exponentially away along the x axis (or, more generally, along the extensional axis). This motion makes it unlikely for particles to move across the compressional axis and cross the associated separatrix ($x = 0$), unless their initial momentum is set in a way that forces such a crossing (see details in Appendix C). In contrast, the eigenvalues $\lambda_c^{\pm}$ can be either real or complex, depending on parameter values, as shown in Figs. 3(c), 3(d), 3(g), and 3(h). When $\lambda_c^{\pm}$ are complex conjugates, the solution in equation (13b) shows that particle trajectories will exhibit oscillatory behavior along the y axis (or, in general, along the compressional axis). As a result, particles may be able to cross the extensional separatrix axis ($y = 0$) in finite time. To determine when $\lambda_c^{\pm}$ becomes complex, we consider the discriminant $\mathfrak{D}_2 = (R/\mathrm{St})^2 - 4(R/\mathrm{St}) + 12(1-R)$. The eigenvalues become complex if the Stokes number lies

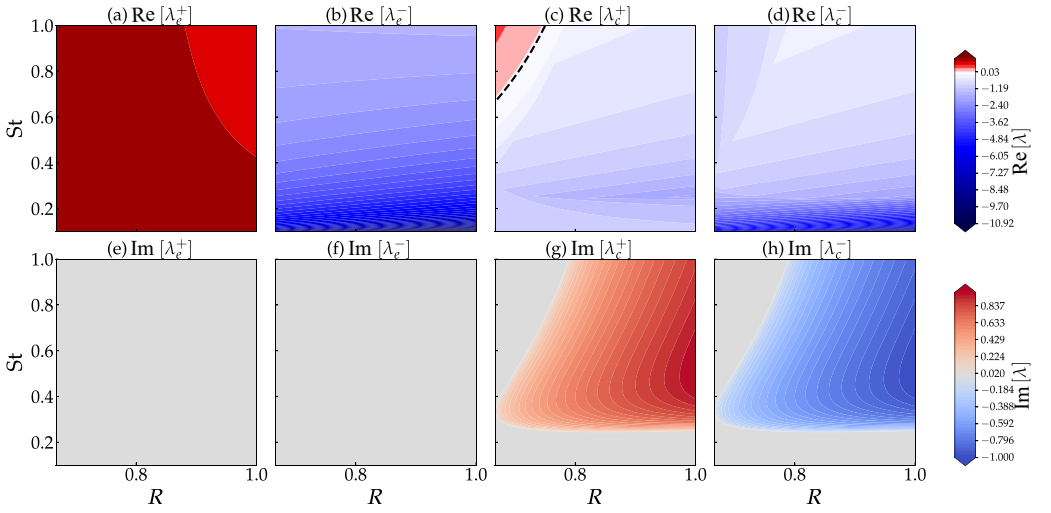

FIG. 3. The real (Re) and imaginary (Im) parts of the eigenvalues $\lambda_e^{\pm}$ and $\lambda_c^{\pm}$ are presented as colored contour plots in the St-R parametric plane. Zero contour lines are highlighted in black dashed in subplot (c).

within the range $\mathrm{St}_c^+ < \mathrm{St} < \mathrm{St}_c^-$, where the critical Stokes numbers are given by

$$\mathrm{St}_c^{\pm} = \frac{R}{2(1 \pm \sqrt{3R-2})}. \tag{14}$$

For $\mathrm{St} \in (\mathrm{St}_c^+, \mathrm{St}_c^-)$, the oscillatory motion allows particles to cross the extensional axis without requiring additional conditions. For the Stokes numbers beyond this critical range, where particle trajectories in phase space become purely exponential, separatrix crossing can only occur under specific initial conditions, which we discuss in Appendix C. For instance, in the infinitely heavy particle limit ($R = 1$), these reduce to $\mathrm{St}_c^+ = 1/4$ and $\mathrm{St}_c^- \to \infty$, consistent with earlier studies [23,25,35].

We identify different dynamical regimes in the St-R parameter space based on the behavior of the eigenvalues, as shown in Fig. 4(a). We also show how the eigenvalues ($\lambda_e^{\pm}$, $\lambda_c^{\pm}$) change as the Stokes number St increases from 0.1 to 1.0 for a fixed density ratio R = 0.70 in Figs. 4(b) and 4(c); this trend remains qualitatively similar for any $R \in (2/3, 1)$. Regions A and C manifest similar dynamical behavior, characterized by the property that all eigenvalues ($\lambda_e^+, \lambda_e^-, \lambda_c^+, \lambda_c^-$) are real, displaying signatures $(+, -, -, -)$, as shown in Figs. 4(b) and 4(c), which correspond to a "3:1 saddle" fixed point in the 4D phase space. Conversely, the region delineated by St_c^+ and St_c^-, referred to as region B, exhibits a distinct nature of the eigenvalues, as not all are purely real. While the real parts maintain the signature $(+, -, -, -)$, the imaginary parts assume signatures $(0, 0, +, -)$, as shown in Figs. 4(b) and 4(c), signifying a "spiral 3:1 saddle" in the 4D phase space. Beyond the critical Stokes number St_{c_p}, the real part of λ_c^+ transitions its sign from negative to positive, as can be seen in Fig. 4(b). The region extending beyond St_{c_p}, indicated as region D in Figs. 4(a), has all real eigenvalues, which, however, exhibit distinct signature from those in regions A, B or C, with two eigenvalues being positive and the other two negative $(+, -, +, -)$. This configuration corresponds to a "2:2 saddle" fixed point in the 4D phase space, following the classification nomenclature referenced in Ref. [36]. The distinction between saddle and spiral–saddle fixed points is important. Since the particle dynamics evolve in a 4D phase space, the nature of the fixed points—whether they have purely real eigenvalues (simple saddles) or include some complex conjugate eigenvalues (spiral–saddles)—significantly affects the local trajectory behavior. For simple saddles, trajectories near the fixed point do not exhibit oscillatory behavior, whereas spiral-saddles introduce a spiralling

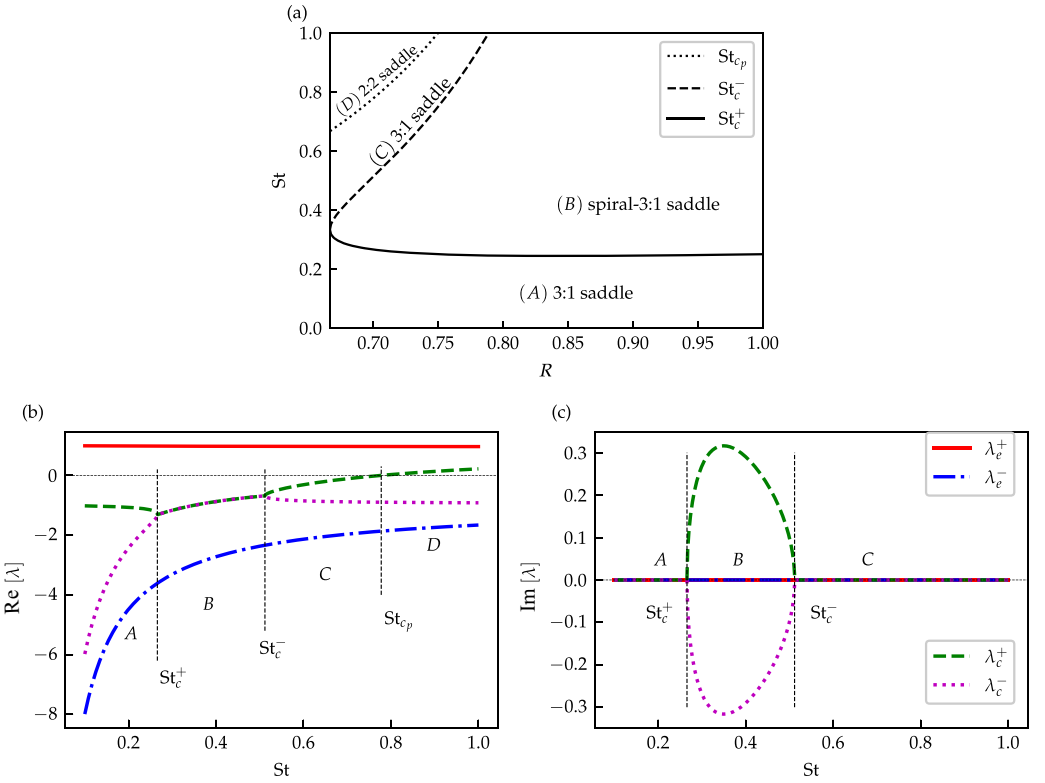

FIG. 4. (a) Different regimes of particle dynamics near a corner fixed point of TG vortex, without history force, are shown in the St-R plane. The critical curves corresponding to St_c^+ (solid line), St_c^- (dashed line), and St_{c_p} (dotted line) mark the boundaries between regions A, B, C, and D. (b) and (c) show the evolution of the real and imaginary parts, respectively, of the four eigenvalues $\lambda_e^{\pm}$ and $\lambda_c^{\pm}$ as functions of St at $R = 0.70$.

motion due to the complex eigenvalues. This spiralling appears as oscillations of trajectories, which can increase the likelihood of trajectories crossing nearby separatrix lines.

In region B, unlike regions A, C, and D, the eigenvalues are complex conjugates, which gives the particle trajectories a spiral shape in phase space. These spirals are attracting because the eigenvalues have negative real parts and nonzero imaginary parts. At the same time, the presence of other real eigenvalues gives the system a saddle-like nature. This combination allows particles to cross the separatrix, a behavior not seen in regions A, C, and D. Still, particles in those regions may also cross the separatrices (along the extensional or compressional axes) if they start with large enough momentum in the right direction (see Appendix C). Also, unlike in regions A and C, where three of the eigenvalues are negative and only one is positive—causing particle trajectories to converge toward the extensional axis over time—in region D, two of the eigenvalues are positive. As a result, this convergence does not occur. Instead, particles tend to move away from the extensional separatrix axis ($y = 0$). This kind of diverging behavior was previously reported by Raju and Meiburg [22], who referred to it as "unphysical." However, we suggest that this change in behavior near the CFPs is actually due to the appearance of EFPs once $\mathrm{St} > \mathrm{St}_{c_p}$. In this parameter range, particles may be more likely to cross the extensional separatrix, depending on their initial conditions. We explore the eigenvalue behavior of EFPs in detail in Sec. III B. To gain further insight into particle dynamics near the CFPs under different parametric regimes and initial conditions, we present analytically computed particle trajectories in linearized TG vortex flow in the physical x-y plane. Particles are initially positioned at $(x,\ y) = (0.1,\ 1)$ in the linearized TG vortex flow (here,

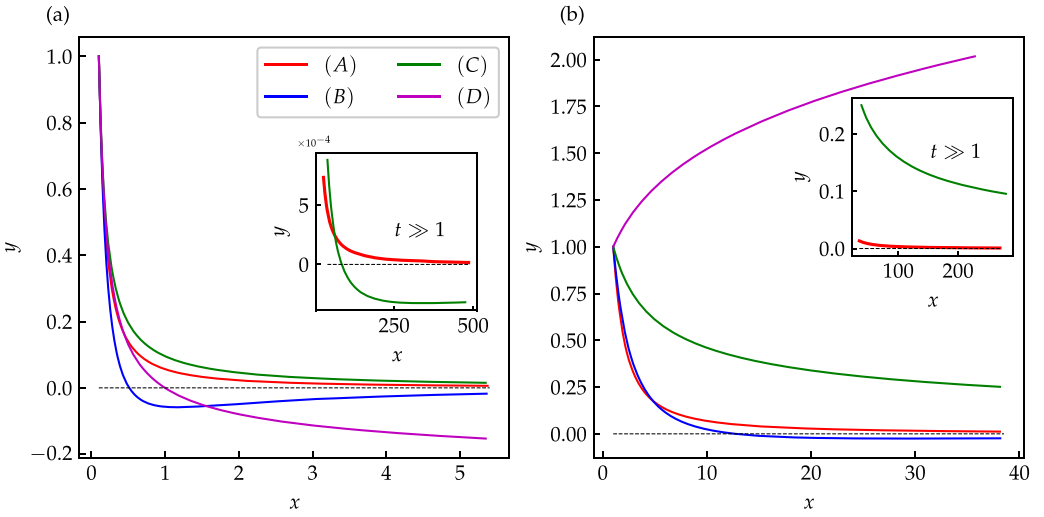

FIG. 5. Particle trajectories representative of each parametric regime are shown for two cases: (a) zero initial slip velocity and (b) zero initial particle velocity. In both cases, particles are initialized near the stagnation point at the origin, specifically at the coordinate location (0.1, 1). The following parameter sets are used to illustrate each regime: region A with $R = 0.8$, $\mathrm{St} = 0.2$; region B with $R = 0.85$, $\mathrm{St} = 0.5$; region C with $R = 0.67$, $\mathrm{St} = 0.45$; and region D with $R = 0.7$, $\mathrm{St} = 1.0$. Insets show zoomed-in views to better visualize the separatrix crossings at the longtime limit.

there is a CFP at the origin). We consider two initial velocity conditions: (i) the particle velocity is set equal to the local fluid velocity—referred to as the zero slip velocity condition (i.e., $\mathbf{v} = \mathbf{u}$); and (ii) the particle starts from rest (i.e., zero initial velocity). Henceforth, "zero slip velocity" denotes that the particle velocity matches the local fluid velocity at the initial instant. Figures 5(a) and 5(b) show the particle trajectories for the zero slip and zero velocity initializations, respectively. As seen in Fig. 5(a), the trajectory in regime A does not cross the extensional separatrix axis ($y = 0$), consistent with the 3:1 saddle nature of the CFP. In contrast, in regime B, the transition of the CFP to a spiral-3:1 saddle facilitates the particles to move across the separatrix line in a finite time. Interestingly, in regime C, the trajectory also intersects the separatrix, albeit at long times ($t \gg 1$) [see Fig. 5(a)], despite the eigenvalue characteristics of the fixed point being similar to regime A. This confirms that particle crossing of the separatrix can occur without oscillatory behavior, depending on the appropriate initial conditions and parameter values, as discussed in Appendix C. In regime D, again the particle trajectory is able to cross the extensional separatrix line, aided by the appropriate initialization. Here, the CFP exhibits 2:2 saddle characteristics, and thus, after the crossing, the trajectory is advected away from the separatrix due to two positive eigenvalues. This contrasts with regimes A, B, and C, where particle trajectories—whether they cross the separatrix or not—eventually align with it in the long time limit.

In the second scenario where particles are initially at rest (i.e., with zero initial velocity), the trajectories corresponding to regimes A and B display similar qualitative behaviors as before: particles in regime A remain confined, exhibiting trapping behavior, whereas those in regime B cross the extensional separatrix line ($y = 0$), as shown in Fig. 5(b). In this case, the trajectories associated with regime C no longer intersect the separatrix, consistent with the underlying eigenvalue characteristics. However, this behavior contrasts with the zero slip velocity case in Fig. 5(a), where particles from regime C were able to cross the separatrix at long times ($t \gg 1$) due to their sufficient initial momentum, which is absent in the setup here. Furthermore, particles from regime D now move against the flow direction and fail to cross the extensional separatrix line, again due to the lack of appropriately directed initial momentum (see Appendix C). As before, trajectories

in regimes A, B, and C asymptotically align with the extensional separatrix axis at long times. In contrast, the trajectory from regime D aligns along a different direction, governed by the presence of two positive eigenvalues that direct the particle away from the separatrix.

Note that we have discussed extensively whether particle trajectories can cross the separatrix lines in this section, and we will continue to explore this in subsequent sections. Understanding whether particles cross separatrix lines near fixed points is crucial, as such crossings indicate leakage from the initial vortex cell into neighboring ones, ultimately leading to enhanced particle dispersion in the full TG vortex flow. In a more general context, the deposition and transport patterns governed by separatrix crossing are fundamental to a range of applications, including aircraft icing, aerosol transport, and microfluidic particle sorting. The influence of separatrix crossing plays a pivotal role in determining particle or droplet deposition in fluid flows around immersed bodies. The possibility of droplets crossing these separatrices and impacting the surface is central to predicting ice accretion patterns on aircraft wings [25]. Crucially, identifying the critical parametric threshold—often characterized by a critical Stokes number—delineates the regimes of particle capture and escape near a bluff body and is highly sensitive to both the underlying flow topology and particle inertia [37]. In this direction, expressions for the critical Stokes number required for separatrix crossing have been established in earlier studies (see, e.g., Refs. [25,37–41]). Recall that our analysis in this section focuses on particle dynamics in the vicinity of fixed points in the TG vortex flow, where we approximate the flow as a simple stagnation flow through linearization. Consequently, we should ideally consider small values of x and y. However, as shown in the insets of Figs. 5(a) and 5(b), the use of large values (e.g., on the order of 10^2) extends beyond this intended context. These large values are primarily included to illustrate the behavior of particles in an unbounded straining flow. In the context of the TG vortex flow, by the time particles are predicted to cross the separatrix axes, they may already be sufficiently far from the fixed point such that the nonlinearity of the TG vortex flow can no longer be neglected. Consequently, the predictions may differ when accounting for this nonlinearity. Furthermore, once a particle crosses a separatrix of the TG vortex flow, the nonlinear flow in the adjacent vortex cell may carry it further away from the fixed point, with nonlinear effects ultimately governing its subsequent dynamics—potentially guiding it toward another fixed point.

B. Particle dynamics near an edge fixed point of the TG vortex flow—Without history force

The effective flow field is merely a construct that represents the modified flow perceived by an inertial particle. Despite this representation, inertial particles will behave differently from streamlines in this effective flow field due to their finite inertia. To completely understand inertial particle dynamics, one must linearize the full governing system of equations, such as Eqs. (7) or (8), about the fixed points in the phase space. Once the EFPs exist, the local flow field in their vicinity resembles that of a linear extensional flow, consistent with their kinematic saddle-type nature, as demonstrated in Appendix A. Consequently, they possess extensional and compressional axes, which would be appropriately switched for other EFPs. Therefore, without loss of generality, as in Sec. III A, we can focus on one of the EFPs, let us say the one at $(\cos^{-1}[-\gamma],\ 0)$ in the basic vortex cell. We linearize Eqs. (8a) and (8b) about this fixed point, yielding the following simplified governing equations:

$$\frac{\mathrm{St}}{R}\,\ddot{x} + \dot{x} - (\gamma - \gamma^{-1})\,x = 0, \tag{15a}$$

$$\frac{\mathrm{St}}{R}\,\ddot{y} + \dot{y} - (\gamma + \gamma^{-1})\,y = 0. \tag{15b}$$

As expected for an inertial particle in any saddle-like flow field, the system reduces to two independent linear harmonic oscillators. Consequently, the solution can be expressed as a linear

combination of exponential functions, similar to Eqs. (13), albeit with different eigenvalues and integration constants. The eigenvalues in this case are

$$\lambda_1^{\pm} = \frac{1}{2\,\mathrm{St}}\left[-R \pm \sqrt{R\,(R + 4\,\mathrm{St}\,(\gamma - \gamma^{-1}))}\right], \tag{16a}$$

$$\lambda_2^{\pm} = \frac{1}{2\,\mathrm{St}}\left[-R \pm \sqrt{R\,(R + 4\,\mathrm{St}\,(\gamma + \gamma^{-1}))}\right]. \tag{16b}$$

Similar to the case of corner fixed points in Sec. III A, here, the eigenvalues corresponding to the EFPs also exhibit a transition in behavior in the parametric plane. The eigenvalues $\lambda_2^{\pm}$ remain purely real for all relevant parameter regimes, with λ_2^{+} always positive and λ_2^{-} always negative. However, the eigenvalues $\lambda_1^{\pm}$ can be purely real and negative for certain parameter regimes but transition into complex conjugate pairs with a negative real part when the Stokes number exceeds a critical value. This critical Stokes number can be determined by setting the discriminant of $\lambda_1^{\pm}$ in Eq. (16a) to zero, yielding $R + 4\,\mathrm{St}\,(\gamma - \gamma^{-1}) = 0$. Solving for St, we obtain the critical Stokes number as

$$\mathrm{St}_{c_2} = \frac{R\sqrt{7 - 3R}}{6\,(1 - R)}. \tag{17}$$

Consequently, the nature of inertial particle trajectories near the EFPs in phase space corresponds to a 3:1 saddle when $\mathrm{St} < \mathrm{St}_{c_2}$, transitioning to a spiral-3:1 saddle when $\mathrm{St} > \mathrm{St}_{c_2}$. It is also important to note that these EFPs exist only if $\mathrm{St} > \mathrm{St}_{c_p}$. Similar to the case of CFPs, the emergence of spiral characteristics in the phase-space trajectories shows enhanced particle leakage in the vicinity of these EFPs when $\mathrm{St} > \mathrm{St}_{c_2}$.

In Fig. 6(a), the magenta dashed-dotted curve represents the critical line $\mathrm{St}_{c_p} = R/\{3\,(1 - R)\}$ in the St-R parametric plane, marking the threshold above which EFPs emerge. This region coincides with region D in Fig. 4(a), where the behavior of the CFPs transition from 3:1 saddle to 2:2 saddle. This region is further divided into two subregions, D_1 and D_2, by the cyan dashed curve corresponding to St_{c_2}. As previously discussed, in region D_1, the trajectories of inertial particles near the EFPs in the 4D phase space exhibit a 3:1 saddle behavior, characterized by real eigenvalues with signatures $(+, -, -, -)$, as shown in Fig. 6(b). In region D_2, as illustrated in Fig. 6(a), the nature of the edge fixed points transitions to a spiral-3:1 saddle configuration, due to one pair of complex conjugate eigenvalues $\lambda_1^{\pm}$, while the real parts of all eigenvalues retain the same signature as in region D_1. Figures 6(b) and 6(c) show the typical variation of both the real and imaginary components of these eigenvalues with the Stokes number for $R = 0.67$. In fact, these plots simultaneously represent all four eigenvalues associated with both a typical EFP and CFP. As indicated, the EFPs emerge only for $\mathrm{St} > \mathrm{St}_{c_p}$, whereas the CFPs persist throughout the entire range of St.

Although our primary interest lies in the range $R \in (2/3, 1)$, the parametric plot in Fig. 6(a) has been extended to the broader range $R \in (0, 1)$ to illustrate the generality of our results. The regions A and C merge into a single domain for lighter particles ($R < 2/3$). As discussed earlier, the CFPs display a 3:1 saddle behavior as long as the Stokes number stays below the threshold St_{c_p}. When the Stokes number exceeds St_{c_p}, the dynamics of CFPs shift to a 2:2 saddle configuration with eigenvalue signatures $(+, -, +, -)$ while the EFPs exhibit 3:1 saddle behavior with eigenvalue signatures $(+, -, -, -)$ as shown in Figs. 6(a)–6(c). Figure 6(a) illustrates this behavior in the St-R parameter space, where the grey color marks the critical boundaries corresponding to the CFPs. For lighter particles as well, the EFPs continue to exist for Stokes numbers greater than St_{c_p}, showcasing 3:1 saddle characteristics in regime D_1. As the Stokes number increases beyond St_{c_2}, the characteristics of EFPs transition to a spiral 3:1 saddle configuration. Meanwhile, the CFPs retain their 2:2 saddle behavior throughout this parameter regime.

At $\mathrm{St} = \mathrm{St}_{c_p}$, an EFP emerges from a CFP, marking a transition in the CFP's nature from a 3:1 saddle to a 2:2 saddle. This transition corresponds to a saddle-node bifurcation, as the product of eigenvalues becomes zero [42]. At a different critical value $\mathrm{St} = \mathrm{St}_{c_2}$, the behavior of EFP transitions from a 3:1 saddle to a spiral 3:1 saddle, while the CFP continues to exhibit 2:2 saddle

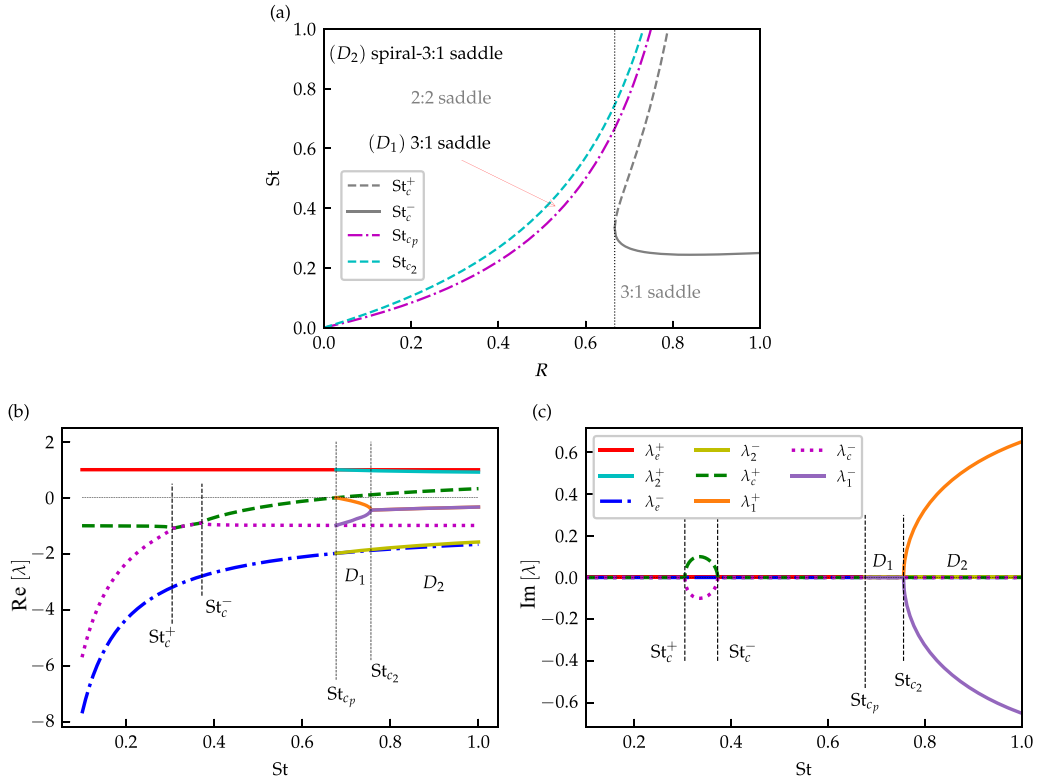

FIG. 6. (a) Different regimes of particle dynamics near an edge fixed point of the TG vortex, without the history force, are shown in the St-R plane. The magenta, dash-dotted curve corresponds to the critical line St_{c_p}, marking the threshold above which region D emerges, where edge fixed points exist. The cyan dashed curve, corresponding to St_{c_2}, further divides this region into subregions D_1 and D_2. For comparison, the other critical curves—associated with corner fixed points—that separate regions A, B, and C from D are also shown in grey in the background. (b) and (c) show the evolution of the real and imaginary parts, respectively, of the eigenvalues $\lambda 1^{\pm}$ and $\lambda_2^{\pm}$ associated with the edge fixed points, as functions of St at $R = 0.67$. For comparison, the eigenvalues $\lambda_e^{\pm}$ and $\lambda_c^{\pm}$ associated with corner fixed points are also included.

behavior. Since this change involves only a modification in the dynamical nature of the EFP and not the appearance or disappearance of fixed points, it is not classified as a bifurcation. These transitions are best illustrated in Fig. 7, where dots and stars denote the eigenvalues of CFPs and EFPs, respectively. In Fig. 7(a), for $\mathrm{St} < \mathrm{St}_{c_p}$, only CFPs are present with eigenvalue signature $(+, -, -, -)$, indicating 3:1 saddle behavior. In Fig. 7(b), just beyond St_{c_p}, EFPs emerge with eigenvalue signature $(-, -, +, -)$, while the CFP signature changes to $(+, -, +, -)$, confirming the occurrence of a saddle-node bifurcation. As St approaches St_{c_2}, the eigenvalues associated with the CFP remain qualitatively unchanged, while the two real eigenvalues of the EFP coalesce and transition into a pair of complex conjugates, leading to their spiral 3:1 saddle behavior, as shown in Figs. 7(c) and 7(d).

C. Particle dynamics near a corner fixed point of the TG vortex flow—With history force

Here, as an extension of the previous subsection Sec. III A, we consider particle motion near a typical CFP of the TG vortex flow while accounting for the history force. As before, the governing Eqs. (5) can be simplified in the vicinity of the CFP. Without loss of generality, we focus on the

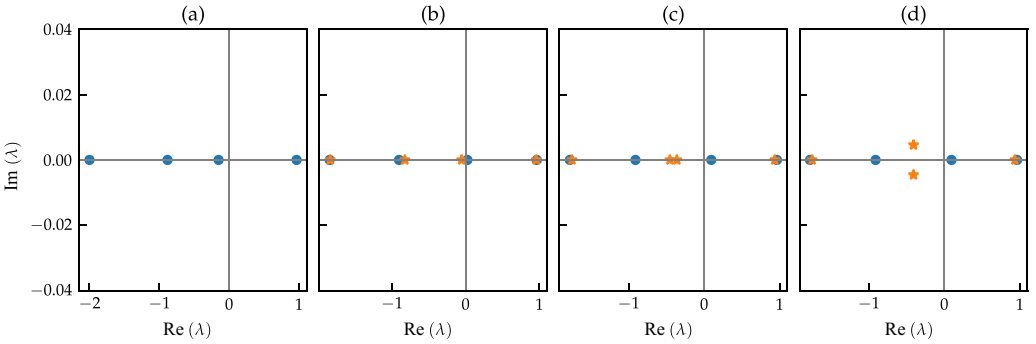

FIG. 7. Evolution of eigenvalues associated with corner and edge fixed points in the complex plane (real versus imaginary plane) as the Stokes number varies across critical values, at fixed $R = 0.67$: (a) $\mathrm{St} < \mathrm{St}_{c_p}$, (b) $\mathrm{St} > \mathrm{St}_{c_p}$, (c) $\mathrm{St} < \mathrm{St}_{c_2}$, and (d) $\mathrm{St} > \mathrm{St}_{c_2}$. Blue dots and orange stars mark the eigenvalues associated with the corner fixed points and the edge fixed points, respectively.

fixed point at the origin of the TG vortex flow, and retaining the history force, yielding the linear version of the governing equations as

$$\ddot{x} + \frac{\mathrm{R}}{\mathrm{St}}\dot{x} - x\left(3\,(1-\mathrm{R}) + \frac{R}{\mathrm{St}}\right) = -\frac{\kappa}{\sqrt{\pi}}\left[\frac{\dot{x}_0 - x_0}{\sqrt{t}} + \int_0^t \frac{1}{\sqrt{t-t'}}\left(\frac{d^2x}{dt'^2} - \frac{dx}{dt'}\right)dt'\right], \quad (18a)$$

$$\ddot{y} + \frac{\mathrm{R}}{\mathrm{St}}\dot{y} - y\left(3\,(1-\mathrm{R}) - \frac{R}{\mathrm{St}}\right) = -\frac{\kappa}{\sqrt{\pi}}\left[\frac{\dot{y}_0 + y_0}{\sqrt{t}} + \int_0^t \frac{1}{\sqrt{t-t'}}\left(\frac{d^2y}{dt'^2} + \frac{dy}{dt'}\right)dt'\right]. \quad (18b)$$

Recall that x_0, y_0, $\dot{x}_0$, and $\dot{y}_0$ denote the initial positions and velocities of the particles, respectively. These equations are integrodifferential in nature and do not represent a simple dynamical system, like Eqs. (12). Although the left-hand sides of both systems remain identical, the right-hand sides differ due to forcing terms associated with the memory effect of the particle's dynamical history. Here, this memory term appears as an integral. In the infinitely heavy particle limit ($R \to 1$), both systems exhibit similar dynamical behavior since the coefficient of the history term, κ, defined in Eq. (6), approaches zero. Despite these complexities, the system in Eqs. (18) remains linear, and the dynamics in the x and y directions remain decoupled, allowing analytical solutions through methods such as the classical Laplace transform. The solutions to Eqs. (18) in the Laplace domain are given by

$$\hat{x} = \frac{1}{\prod_{i=1}^{4}(\sqrt{s} - \mu_{x_i})}\left(s\,x_0 + \kappa\sqrt{s}\,x_0 + \frac{R}{\mathrm{St}}x_0 + \dot{x}_0\right), \quad (19a)$$

$$\hat{y} = \frac{1}{\prod_{i=1}^{4}(\sqrt{s} - \mu_{y_i})}\left(s\,y_0 + \kappa\sqrt{s}\,y_0 + \frac{R}{\mathrm{St}}y_0 + \dot{y}_0\right). \quad (19b)$$

Here, $\hat{x}$ and $\hat{y}$ are the Laplace transforms of the variables x and y, respectively, while μ_{x_i} and μ_{y_i} are the roots of the quartic polynomials $P_1(\xi) = \xi^4 + \kappa\,\xi^3 + (R/\mathrm{St})\,\xi^2 - \kappa\,\xi - [R/\mathrm{St} + 3(1-R)]$ and $P_2(\xi) = \xi^4 + \kappa\,\xi^3 + (R/\mathrm{St})\,\xi^2 + \kappa\,\xi - [3(1-R) - R/\mathrm{St}]$, respectively. The roots μ_{x_i} and μ_{y_i} are independent of initial conditions and can be uniquely determined for given values of St and R. Applying partial fraction decomposition and performing the inverse Laplace transform on Eqs. (19), we obtain the general solutions for the particle trajectories x and y as

$$x(t) = \Sigma_{i=1}^{4} A_{x_i}\mu_{xi}\exp\left(\mu_{x_i}^2 t\right)\mathrm{erfc}(-\mu_{x_i}\sqrt{t}), \quad (20a)$$

$$y(t) = \Sigma_{i=1}^{4} A_{y_i}\mu_{y_i}\exp\left(\mu_{y_i}^2 t\right)\mathrm{erfc}(-\mu_{y_i}\sqrt{t}). \quad (20b)$$

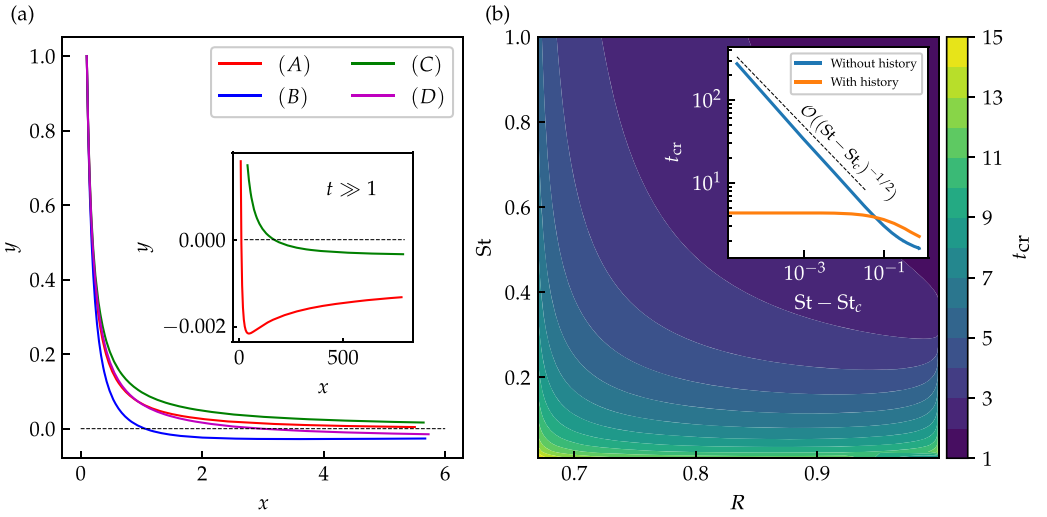

FIG. 8. (a) Typical particle trajectories near a corner fixed point (at the origin) under the influence of the history force. Particles are initialized at location (0.1, 1) with zero initial slip velocity for different parameter combinations: region A with $R = 0.8$, $\mathrm{St} = 0.2$; region B with $R = 0.85$, $\mathrm{St} = 0.5$; region C with $R = 0.67$, $\mathrm{St} = 0.45$; and region D with $R = 0.7$, $\mathrm{St} = 1.0$. The zoomed-in inset shows particle trajectories at $t \gg 1$ for regions A and C. (b) Colored contour plot of first crossing time t_{cr} associated with a particle initialized at (0.1, 1) with zero slip velocity, is shown in the St–R parameter space, accounting for the history force. The inset plot of panel (b) compares the variations of t_{cr} with $\mathrm{St} - \mathrm{St}_c$ under scenarios both with and without the influence of the history force. The resultant curve obtained in the absence of history force exhibits a power law scaling behavior characterized by the singular relationship $(\mathrm{St} - \mathrm{St}_c)^{-1/2}$.

The coefficients A_{x_i} and A_{y_i} depend on the initial conditions, the roots μ_{x_i} and μ_{y_i}, as well as the parameters St and R. They are given by

$$A_{x_i} = \frac{x_0\left(\mu_{x_i}^2 + \kappa\mu_{x_i}\right) + \frac{R}{\mathrm{St}}x_0 + \dot{x}_0}{\prod_{j\neq i,j=1}^{j=4}\left(\mu_{x_i} - \mu_{x_j}\right)}; \quad \Sigma_{i=1}^{4} A_{x_i} = 0, \tag{21a}$$

$$A_{y_i} = \frac{y_0\left(\mu_{y_i}^2 + \kappa\mu_{y_i}\right) + \frac{R}{\mathrm{St}}y_0 + \dot{y}_0}{\prod_{j\neq i,j=1}^{j=4}\left(\mu_{y_i} - \mu_{y_j}\right)}; \quad \Sigma_{i=1}^{4} A_{y_i} = 0. \tag{21b}$$

The complementary error function (erfc) in the general solution, along with the exponential terms, captures the influence of the history force. Analyzing the roots of the characteristic polynomials $P_1(\xi)$ and $P_2(\xi)$ provides insights into particle trajectories, though this can be complex. For long times ($t \gg 1$), particle trajectories generally tend toward the extensional axis (here, $y = 0$) at a rate of $t^{-1/2}$, unless the real parts of the roots μ_{y_i} are significantly large and positive. This implies that, compared to cases without history effects, particles approach the extensional separatrix line ($y = 0$) at a slower rate. However, whether the trajectories cross this line remains uncertain and requires further analysis. Determining this would involve solving Eq. (20b) for the time at which $y(t) = 0$, but this is analytically challenging and is not pursued here. Instead, a numerical investigation of this aspect is presented later in this section. To examine the effect of the history force on particle trajectories, we present representative trajectories for different parameter combinations, all initialized at location $(x,\ y) = (0.1,\ 1)$ near the stagnation zone with zero initial slip velocity, as shown in Fig. 8(a). The parameter combinations used here are the same as in Fig. 5, but only the zero initial slip velocity case is considered. The selected trajectories correspond to the typical parametric conditions from distinct regions A, B, C, and D of the St-R parameter space, as discussed in the previous section. Particles originating from all distinct dynamical regions A, B, C, and D cross the

extensional separatrix axis ($y = 0$ line) in finite time and eventually align parallel to this axis at long times, as illustrated in Fig. 8(a). Notably, particles from region D, which failed to align in the absence of history force [see Fig. 5(a)], now exhibit this aligning behavior when the history force is included. Here, the history force counteracts the misalignment introduced by the added mass and pressure gradient effects. Additionally, an important difference here is observed in region A: with the history force, particles cross the extensional separatrix line, a phenomenon not seen when the history force is absent.

As discussed in the previous subsections, particles to cross the compressional separatrix ($x = 0$ line) remain challenging and typically require them to possess specific initial momentum. In contrast, the oscillatory nature of particle trajectories more easily enables them to cross the extensional separatrix ($y = 0$ line). To investigate whether particles do so under the influence of the history force, we employ a numerical root-finding method to solve for $y(t) = 0$, as finding an explicit analytical solution for the crossing time from Eq. (20b) is nontrivial. Using the analytical expression in Eq. (20b), we track the trajectory of a particle initialized at $y_0 = 1$ with zero slip velocity, and numerically find the time at which the trajectory crosses the $y = 0$ line. To accomplish this, we detect a change in the sign of $y(t)$ by employing Brent's method implemented via the "brentq" function in Python's SciPy library. The first occurrence of such a crossing is recorded and defined as the "first crossing time," t_{cr}. This process is repeated for a range of parameter combinations, and the results are presented as a colored contour plot in the St-R plane in Fig. 8(b). The results show that for all parameter combinations considered, particles with history force eventually cross the extensional axis in a finite time, indicating that the history effect removes the critical threshold required for particles to cross separatrix lines, in agreement with earlier findings by Druzhinin and Ostrovsky [30]. However, t_{cr} varies with St and R, with shorter crossing times in some regions (indicated by blue) and longer crossing times in others (yellow). Specifically, particles with low St values and R close to 0.67 take significantly longer to cross the separatrix compared to those with high St values and R near 1, as evident from Fig. 8(b). Additionally, as $R \to 1$, this first crossing time is large for $\mathrm{St} < 1/4$ but reduces for $\mathrm{St} > 1/4$, consistent with results in the absence of the history force. Notably, unlike the case without history effects, no subregions within the parameter space indicate permanent trapping of particles near the fixed point when the history force is considered.

Near a stagnation region, as we have seen in this section, particles that cross the separatrices may eventually align along the extensional axis over long timescales. However, in the full TG vortex flow—which is spatially nonlinear—such particles are typically advected away from the stagnation region due to the influence of neighboring vortical structures and flow nonlinearities. Therefore, the first crossing time (t_{cr}) serves as a useful measure of how rapidly particles escape from the entrainment zone enclosed by the flow separatrices.

As the Stokes number approaches the critical value St_c, defined in Eq. (14), at a given R, the first crossing time diverges in the absence of history force. Conversely, the curve representing the critical crossing time (t_{cr}) manifests a smooth variation in the presence of the history force. The inset in Fig. 8(b) illustrates a comparison of the t_{cr} curve as it varies with the difference $(\mathrm{St} - \mathrm{St}_c)$, both with and without the consideration of history force. It is observed that the divergence of t_{cr} in the absence of history force near the critical Stokes number St_c adheres to a $-1/2$ scaling law with respect to $(\mathrm{St} - \mathrm{St}_c)$, assuming that the particles are initialized with zero slip velocity.

IV. PARTICLE DYNAMICS IN THE FULL NONLINEAR TG VORTEX FLOW—WITHOUT HISTORY FORCE

In Sec. III, we have analyzed the dynamics of inertial particles near the fixed points of the TG vortex flow and examined the critical criteria associated with particle leakage across flow separatrices. The governing dynamical equations became linear since the flow field was locally linear near these fixed points, making the analysis analytically tractable and relatively straightforward. We have even explained the longtime dynamics of particles in these linearized flow structures. However, once particles leak across the flow separatrices, they traverse the nonlinear TG vortex flow

structures before encountering another fixed point/stagnation region. Hence, a comprehensive study of the full nonlinear system is necessary to understand the complete particle dynamics in the TG vortex flow. Due to the nonlinear nature of the governing equations, an analytical approach becomes challenging, necessitating numerical methods. In this section, we investigate the dynamics of inertial particles in the TG vortex flow without history force effects, while considering the pressure gradient force and added mass effects, by numerically solving the governing equations [Eqs. (7)]. As these equations form a set of coupled, nonlinear ordinary differential equations, we employ a fourth-order Runge–Kutta scheme for numerical integration.

To utilize the periodic nature of the flow field, we seed 10^4 particles uniformly within the basic vortex cell $(0, \pi) \times (0, \pi)$ and track their trajectories by integrating the governing equations [Eqs. (7a) and (7b)] from $t = 0$ to $t = 10^4$ nondimensional time units. This study specifically focuses on the dynamics of heavier particles rather than lighter ones. Consequently, the density parameter R is varied within the range $2/3$ to 1, while the Stokes number is restricted to values less than or equal to 1 for simplicity. To characterize the dispersion behavior of the particles, we compute the mean (averaged over all particle trajectories) square displacement (MSD), defined as

$$\text{MSD} = \langle \, \|\mathbf{x}(t) - \mathbf{x}_0\|^2 \, \rangle, \tag{22}$$

Here, $\langle \cdot \rangle$ denotes the average over all particle trajectories $\mathbf{x}(t)$, each originating from an initial position $\mathbf{x}(t = 0) = \mathbf{x}_0$, while $\| \cdot \|$ represents the 2-norm. The longtime scaling behavior of MSD with time, given by MSD $\sim t^n$, characterizes the mean particle dispersion. If particle dispersion is dominated by diffusion, then the exponent is $n = 1$; if ballistic motion dominates, then $n = 2$; and if particles exhibit limited dispersion due to trapping, then $n = 0$. This MSD-based classification also provides a way to distinguish between regular (nonchaotic) and chaotic particle dynamics. Following earlier studies by Wang *et al.* [21] and Nath *et al.* [23,24], we can consider both trapped ($n = 0$) and ballistic ($n = 2$) behaviors to be indicative of regular motion, as the corresponding trajectories are typically structured and predictable, like limit cycles or periodic open trajectories. In contrast, the diffusive regime ($n = 1$)—arising from irregular, random-walk-like transitions across separatrices and vortex cells—is in general associated with chaotic dynamics. The study by Wang *et al.* [21] examined the dynamics of inertial particles in the TG vortex flow, excluding history effects, and identified regions of regular and chaotic motion in the St-R parameter space. However, in their analysis, they employed an older form of the added mass term, similar to that in the original Maxey-Riley equation [6], which effectively introduces an additional term, $(1 - R)\,(\mathbf{v} - \mathbf{u}) \cdot \boldsymbol{\nabla}\mathbf{u}$ to the equations of motion in Eq. (1), thereby altering the form of Eqs. (7). The authors considered particles with St $\lesssim 12$ and R in the range (0.8,0.975), reporting that particles with higher St and lower R exhibit diffusive dispersion at long times due to chaotic (random walk-like) trajectories ($n \approx 1$). Conversely, particles in other regimes display regular motion, leading to either open ($n \approx 2$) or closed trajectories ($n \approx 0$), which correspond to ballistic or trapped dispersion, respectively. To assess the influence of the correct form of the added mass term on particle dynamics and dispersion, we first reproduce the results of Wang *et al.* [21] using our corrected governing equations [Eqs. (7)] for the TG vortex flow. This allows us to examine the impact of the proper added mass formulation on longtime particle dispersion. For direct comparison, we also transform their results to align with the parameter definitions of R and St used in this study.

Wang *et al.* [21] numerically obtained the boundary separating regular and chaotic regimes in the parametric plot. We have digitized this boundary from their Fig. 3 and included it as a blue continuous curve here in Fig. 9. Additionally, Fig. 9 presents a color-coded representation distinguishing regions of regular and chaotic particle dynamics based on the corrected added mass term from our study. To achieve this, we track the dynamics of 10^4 particles that we seed uniformly within the basic vortex cell: $(0, \pi) \times (0, \pi)$. We initialize each particle with zero slip velocity. The simulations are performed over a 26×54 discretized grid in the R-St parameter space, where R ranges from 0.67 to 1 and St ranges from 1 to 12. We compute the MSD for each case and extract the corresponding average scaling exponent n. The resulting contour plot of n in Fig. 9 shows that the boundary separating regular and chaotic regions now differs significantly from the

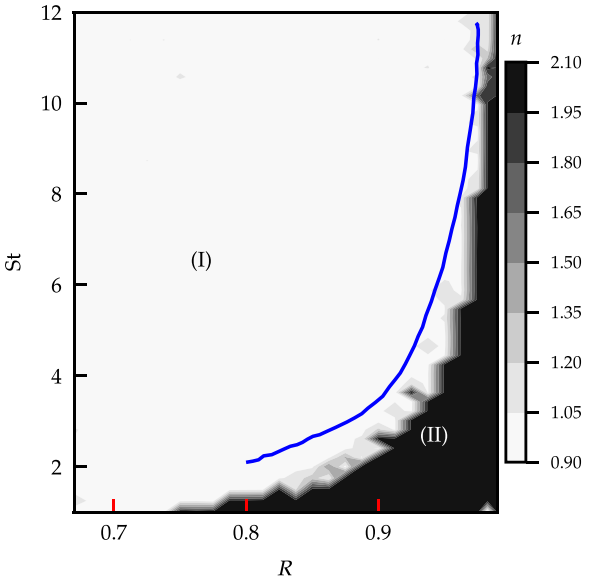

FIG. 9. The regions for chaotic (diffusive) and regular (ballistic) particle motion in the St-R parameter space are demarcated by the blue curve, following the study of Wang *et al.* [21]. Region (I) corresponds to chaotic particle motion, while Region (II) corresponds to regular particle motion. However, as evident from the contour plot, the boundary identified in their study (blue curve) differs from our results.

blue curve reported by Wang *et al.* [21]. Furthermore, this new boundary appears highly irregular. The figure also suggests that the earlier study by Wang *et al.* [21] underestimated the extent of the chaotic region for lower R values ($\sim 2/3$), as we observe chaotic motion even for lower St values (e.g., St < 2) in this regime. In the limit $R \to 1$, as expected the results obtained using the old and corrected forms of the added mass term are almost identical, as the additional term $(1-R)\,(\mathbf{v}-\mathbf{u})\cdot\boldsymbol{\nabla}\mathbf{u}$ from the old formulation becomes negligible, and even the added mass effect itself diminishes.

In Fig. 10(a), we present a contour plot of n in the St-R parameter space, similar to Fig. 9, but extended to focus on the St < 1 range, where more interesting particle dynamics are observed. We identify three distinct regimes in the parameter space, each corresponding to different longtime particle behaviors based on the scaling of MSD with time. The region I in this parametric plot is an extension of the region I in Fig. 9, representing a diffusive regime where particles exhibit chaotic, random-walk-like dispersion ($n \approx 1$). This regime is less pronounced in Fig. 10(a), as it is mostly confined to $R \lesssim 0.75$ and St $\gtrsim 0.7$, but it becomes more dominant over a broader St range in Fig. 9. Similarly, region II in Fig. 10(a) extends region II from Fig. 9, where particle motion is dominantly ballistic ($n \approx 2$). We numerically identify the boundary separating region I (diffusive motion) from region II (ballistic motion), which closely follows the critical Stokes number curve St_{c_p} described in Sec. III. This agreement highlights a direct connection between the onset of EFPs and the transition in longtime dispersion behavior. Interestingly, such connection between local flow structures and global transport behavior is well-studied in the context of Lorentz gas [26], and in flows containing periodic arrays of obstacles or stagnation points [43–45], where the interaction of particles with each individual structure—affecting their escape time—can accumulate over repeated encounters, ultimately leading to anomalous global transport behavior. Below the St_{c_p} curve, EFPs are absent, and particles exhibit regular ballistic motion. Above it, the appearance of EFPs coincides with the onset of chaotic trajectories and diffusive dispersion—a link we suspect to be significant, though not yet fully understood. This transition illustrates how linear stability analysis near fixed points, though inherently local, can capture global dispersion regimes in nonlinear flows. However,

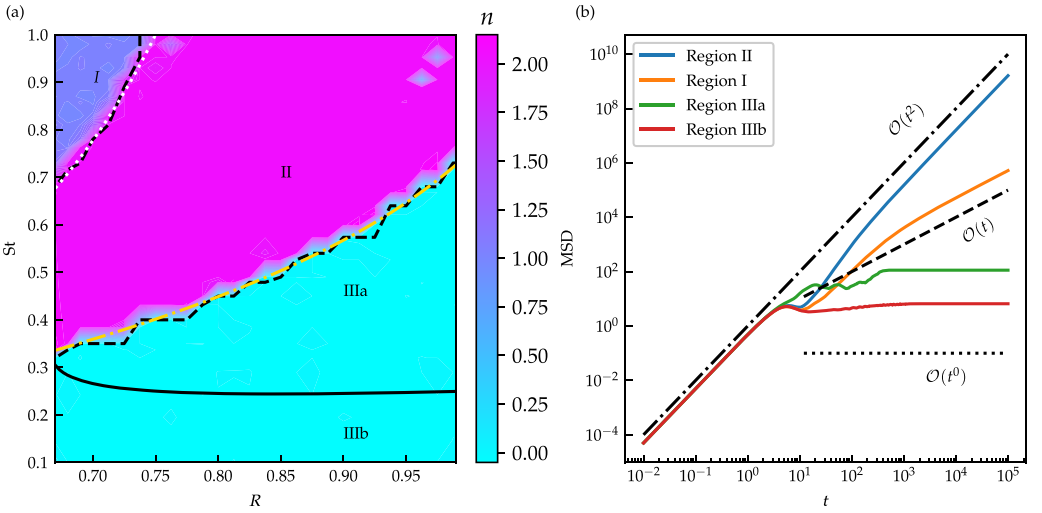

FIG. 10. (a) Regions of diffusive (I), ballistic (II), and trapped (IIIa and IIIb) particle motion are demarcated in the St-R parametric plot, using the colored contour plot of n. The solid black curve denotes the critical Stokes number St_c^+, above which particle trajectories exhibit oscillatory behavior. The yellow dash-dotted line represents St_{c_q}, the threshold below which these oscillations decay eventually. The white dotted curve corresponds to St_{c_p}, marking the onset of EFPs and aligning well with the numerically observed boundary between ballistic and diffusive regimes. (b) MSD versus time plot corresponding to typical parameter combinations from regions I ($R = 0.67, 0.9$), II ($R = 0.7, 0.95$), IIIa ($R = 0.99, 0.7$), and IIIb ($R = 0.7, 0.1$).

unlike in Fig. 9, Fig. 10(a) identifies an additional region, denoted as region III, where particle dispersion is limited, resulting in $n \approx 0$. This region signifies particles that either remain confined by flow separatrices and stagnation regions or are trapped in periodic limit cycle trajectories, as indicated in Ref. [24]. The curve corresponds to St_c^+ divides region III into two subregions. The lower part, the region IIIb, is the same as region A in Fig. 4(a), where particles remain trapped within their initial vortex cell, constrained by separatrices and stagnation regions. Conversely, in the upper part—region IIIa—particles may escape from their initial vortex cell, and subsequently become trapped by the separatrices or stagnation regions of neighboring vortex cells. Particles in region IIIa escape their initial vortex cell through oscillatory motion, but the oscillation amplitude—thus their kinetic energy—diminishes continuously if their Stokes number is below a critical value St_{c_q}, given by

$$\mathrm{St}_{c_q} = \frac{3\,R}{2\,(1+\sqrt{10-9\,R})}. \tag{23}$$

The derivation of Eq. (23) is detailed in Appendix D. The resulting critical threshold, St_{c_q}, shown as a yellow dash-dotted curve in Fig. 10(a), aligns well with the numerically observed boundary separating region IIIa (trapping in a distant vortex cells) from region II (unbounded trajectories). For $\mathrm{St} > \mathrm{St}_{c_q}$, the increasing oscillation amplitudes eventually lead to unbounded particle motion at long times. Alternatively, particles near the boundary curve may evolve into periodic limit cycles, confining them to specific bounded, closed curves. The discrepancy between the numerically observed and analytically derived boundary separating regions II and IIIa may be attributed to the approximations made in Appendix D, particularly the omission of these limit-cycle trajectories from the analysis. In either case—trapped in a limit cycle or trapped by CFPs—the MSD of particles in region IIIa eventually saturates at long times.

Note that Fig. 9 revisits the analysis of Wang *et al.* [21], focusing on how the correct form of the added mass term affects the boundary between regular and chaotic particle motion in the

St-R space. In contrast, Fig. 10(a) extends this by exploring a broader range of particle behaviors, especially when $\mathrm{St} < 1$, delineating regions of trapped, ballistic, and diffusive motion. Thus, while both figures examine transitions between different dynamical regimes, their scopes and aims differ. Figure 10(b) presents the MSD for representative St and R values corresponding to these different regimes. The MSD for region I scales as t, characteristic of diffusive motion, while in region II, it scales as t^2, indicating ballistic transport. In contrast, MSD in regions IIIa and IIIb saturates, though the saturation value is higher in region IIIa, suggesting that particles travel farther from the initial vortex cell before becoming trapped.

Our findings differ from those of Wang *et al.* [21] in two key ways. They reported that in TG vortex flow, diffusion of particles due to their chaotic motion happens only for $\mathrm{St} > 2$ with $R \in (0.8, 1)$, whereas we find diffusion starting at $\mathrm{St} > 0.7$ even when $R \approx 0.67$. Also, while they observed a relatively smooth boundary between regular and chaotic regimes in the parametric space, we find these boundaries to be highly irregular. These differences may be due to their use of a different form of added mass term, which could have affected the results. Another reason could be the limited numerical support and the smaller parameter space they explored. Our study also focuses only on heavier particles and explores the parameter range $R \in (2/3, 1)$. It is possible that similar interesting particle dynamics occur in the regime $R \in (0, 2/3)$, which we have not investigated in this study. We also find that the boundary between region II (ballistic) and region III (trapped) approaches 0.77 as $R \to 1$, consistent with recent findings by Nath *et al.* [24]. Beyond this threshold, particle trajectories transition from a bounded state to an unbounded one for infinitely heavy inertial particles.

When analyzing individual particle trajectories for a given R and St, particularly in region II, we found that some particles initialized within the basic vortex cell exhibit diffusive motion at long times, even though the MSD—the average behavior—identifies this regime as ballistic. This pattern also appears in other regions, where MSD predicts a dominant behavior, but not all particles follow the same longtime dynamics. Instead, some particles exhibit other behaviors, depending on their initial positions and velocities. For instance, even if MSD suggests that particle dispersion should be ballistic for a given St and R in region II, not all particles in the basic vortex cell with these parameter values will necessarily exhibit ballistic motion. When ballistic particles are present, the MSD includes averaging over them, suppressing the contributions of particles following subdominant dynamics (diffusive or trapped), making them less apparent. This suggests that MSD only captures the dominant mean behavior, whereas individual particles may follow different dynamics/dispersion. Note that the scaling of MSD with time tends to be dominated by the fastest-moving particles, which may, however, represent only a small fraction of the total population—as will be evident later in Fig. 11. Such behavior indicates the nonergodic nature of the system, similar to the observation reported by Nath *et al.* [24] for infinitely heavy inertial particles in a TG vortex flow. Our study confirms their findings and extends them to moderately heavy particles. In an ergodic system, a single particle's dynamics and its average over time would match the system's mean behavior over space, allowing mean dynamical studies to be sufficient. However, the absence of ergodicity here means that individual particle dynamics cannot be fully described by MSD alone. Instead, single-particle squared displacement (SD) must be examined to determine how it scales with time at long times.

Following the classification approach of Nath *et al.* [24], for a given St and R, we categorize particles—uniformly initialized at various locations within the basic vortex cell, with zero initial slip velocity—into trapped, diffusive, and ballistic groups based on their long time dispersion behavior, particularly by analyzing the scaling relation $\mathrm{SD} \sim t^n$ as $t \gg 1$. The fractions of each category are shown as contour plots in the St-R parameter space in Figs. 11(a)–11(c). Figure 11(a) indicates that diffusive particles are primarily dominant in region I, with some isolated patches elsewhere. Figure 11(b) shows that ballistic particles dominate region II, though its lower boundary is highly irregular. Figure 11(c) reveals that most trapped particles belong to the region III, though some also appear in regions I and II. Notably, a narrow strip of trapped particles exists in region II, particularly near its lower boundary.

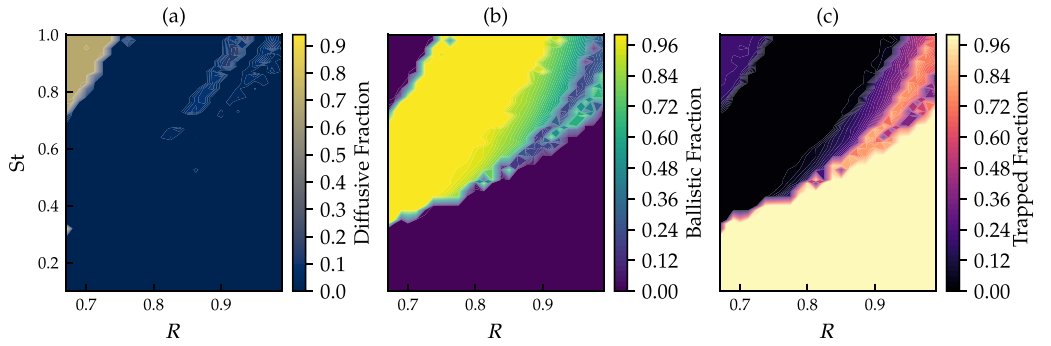

FIG. 11. Fraction of particles exhibiting different types of dynamics: (a) diffusive, (b) ballistic, and (c) trapped, shown as colored contour plots in the St-R parameter space. A total of 10^4 particles are uniformly initialized within the basic vortex cell with zero initial slip velocity, for every St-R combination. Their single-particle SD is evaluated, and its longtime scaling is used to classify the particle behavior and determine the corresponding fractions.

V. EFFECT OF THE HISTORY FORCE ON PARTICLE DYNAMICS IN THE FULLY NONLINEAR TG VORTEX FLOW

In Secs. III A and III B we examined the dynamics of inertial particles near fixed points in the TG vortex flow through linearization. In contrast, the full TG vortex flow without history effects was analyzed in Sec. IV. The influence of the history force on particles only near CFPs in the TG vortex flow (or a general stagnation flow) was considered in Sec. III C. In this section, we conduct a detailed investigation of the effect of the history force on inertial particle dynamics in the fully nonlinear TG vortex flow. Specifically, we explore how the particle dynamics observed in Sec. IV are modified when the history force term is included. To achieve this, we solve the full system of equations [Eqs. (5)]. Since an analytical approach as in Sec. III C is not feasible because of the nonlinearity, we employ numerical methods for this analysis. Including the history force introduces several challenges, even in the numerical integration of the full Maxey–Riley equation. These challenges stem from the singularity of the history kernel $1/\sqrt{t-t'}$, at the upper limit of integration ($t' = t$), and the substantial memory demands due to the history dependence of the integration process. Over the past few decades, researchers have developed various numerical algorithms to address these issues when integrating the Maxey–Riley equation with the history force [5,9,10,33,46–49]. In this section, we numerically integrate our governing equations [Eqs. (5)] using the algorithm proposed in Ref. [49]. In Sec. IV, we identified regions of different particle dynamics in the St-R parameter space in the absence of the history force, as illustrated in Fig. 10(a). Here, we analyze the influence of the history force on particle dynamics in these regions. Figure 12 presents a comparative study, where the central subfigure outlines the different regimes identified in Fig. 10(a), while Figs. 12(a)–12(f) depict single-particle trajectories for representative values of St and R from these regions. Each case includes trajectories both with and without the history force for direct comparison. In all cases, the particles are initialized at identical positions $(0.8,\ 0.8)$ with the same initial velocities, which is zero slip velocity. Figures 12(a)–12(c) correspond to particles that are slightly heavier than the fluid, whereas Figs. 12(d)–12(f) represent cases where the particles are significantly heavier.

For $R = 0.7$ and $\mathrm{St} = 0.2$, as predicted in Sec. III A, the particle is unable to cross the separatrices and confined within the initial vortex cell when the history force is absent. However, upon including the history force, the particle is no longer confined, and is able to cross the separatrices, migrating into neighboring vortex cells, as shown in Fig. 12(c). This behavior is consistent with our findings in Sec. III C, where the inclusion of the history force was shown to eliminate the critical criterion for particle leakage. For $R = 0.7$ and $\mathrm{St} = 0.5$, both with and without the history force, the

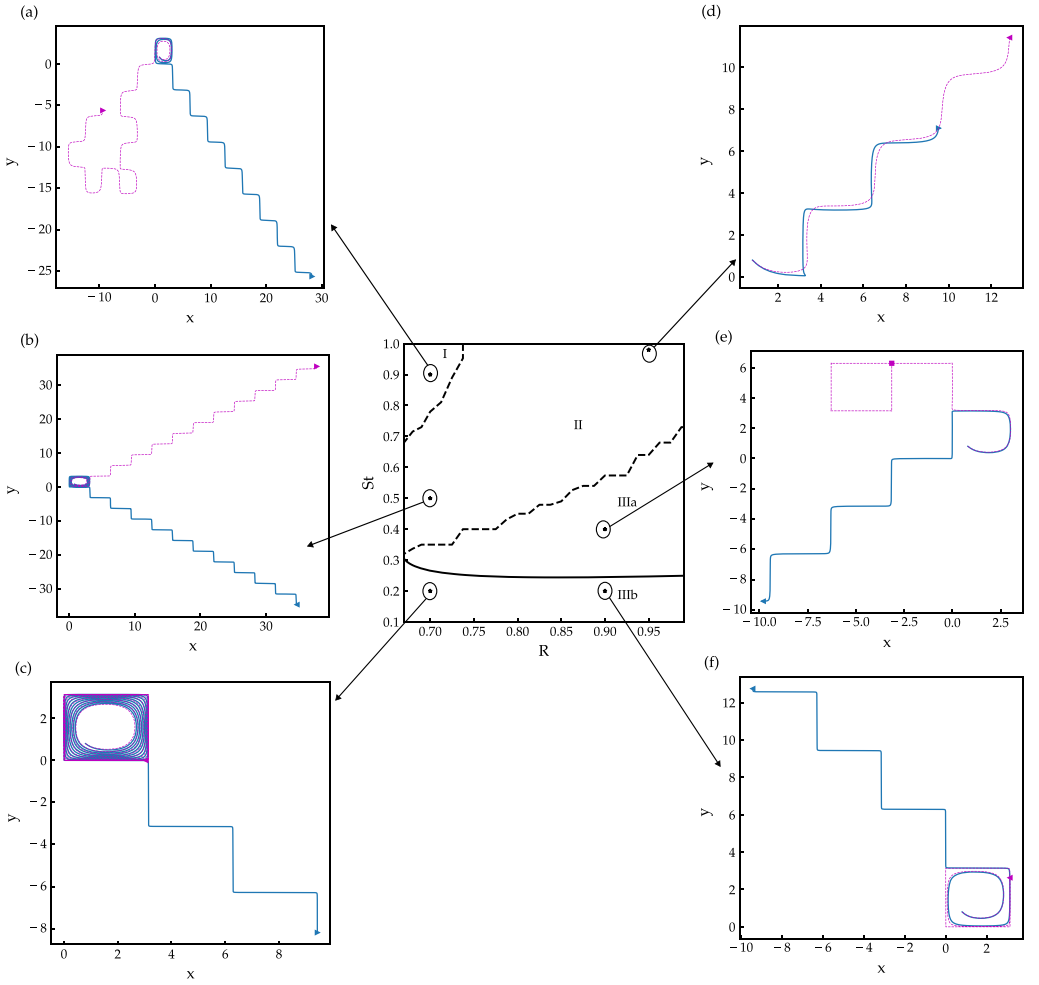

FIG. 12. Typical particle trajectories in the presence of the history force (blue, continuous) are compared with those in the absence of history force (magenta, dashed), for different combinations of St and R. For all the cases, the particles are initialized at the same position (0.8, 0.8) with zero slip initial velocity in the TG vortex flow. The subfigure at the center marks all parametric combinations considered in the St-R plane, which also highlights dynamical regime boundaries (in the absence of the history force) identified in Fig. 10. Panels (a)–(f) compare particle trajectories with and without the history force for the typical parameter combinations in these regimes: (a) $R = 0.7$, St $= 0.9$, (b) $R = 0.7$, St $= 0.5$, (c) $R = 0.7$, St $= 0.2$, (d) $R = 0.95$, St $= 0.98$, (e) $R = 0.9$, St $= 0.4$, and (f) $R = 0.9$, St $= 0.2$. Arrows at the trajectory endpoints indicate continuing motion, while square markers denote particles that have been stopped at those locations.

particle escapes the vortex cell and exhibits ballistic motion at long times, as seen in Fig. 12(b). However, despite identical initial conditions, the two trajectories diverge: the trajectory without the history force follows an average direction of 45°, whereas the trajectory with the history force is directed toward −45°, with the horizontal. This deviation arises due to the history force, which we hypothesize gets amplified when the particle traverses stagnation regions. For $R = 0.7$ and St $= 0.9$, particles without the history force escape the vortex cell and follow chaotic, random-walk-like trajectories, whereas the inclusion of the history force results in regular ballistic motion, as shown in Fig. 12(a).

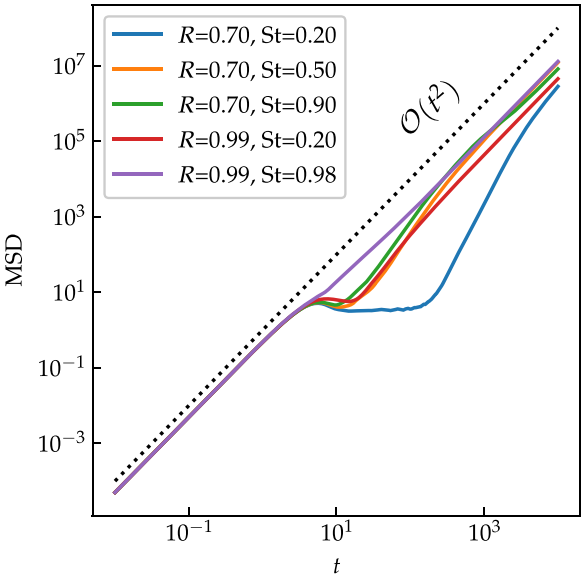

FIG. 13. MSD versus time plot for a few representative combinations of St and R, with history effects included. All particles are initially distributed uniformly within the basic vortex cell with zero initial slip velocity.

Next, we consider the case where particles are significantly heavier than the fluid ($R \geqslant 0.9$). When $R = 0.9$ and $\mathrm{St} = 0.2$, a particle without the history force remains trapped in the vortex cell. However, in the presence of the history force, it escapes, as seen in Fig. 12(f). This behavior is similar to that in Fig. 12(c), even though the influence of the history force is minimal here in the limit of infinitely heavy particles ($R \approx 1$). Also, the spiral part of the trajectory is wider here due to the increased density ratio, even though the Stokes number—and hence the particle inertia—remains the same. For $R = 0.9$ and $\mathrm{St} = 0.4$, a particle without the history force exits its initial vortex cell but becomes trapped in another vortex cell. In contrast, when the history force is included, the particle continues to move without confinement across many vortex cells, as illustrated in Fig. 12(e). Finally, for $R = 0.95$ and $\mathrm{St} = 0.98$, both cases (with and without history) exhibit regular ballistic motion, with trajectories traversing multiple vortex cells, as shown in Fig. 12(d). These ballistic trajectories have the same mean angles from the horizontal, while trajectories with a history force approach the fixed points more closely than those without it.

We report that the inclusion of the history force significantly alters particle dynamics. In this case, particle trapping by flow separatrices no longer occurs, as predicted in Sec. III C. Additionally, all particles exhibit ballistic motion in the longtime limit, irrespective of St, R, or their initial locations. This behavior has been verified for two cases of initial particle velocity: (i) zero initial velocity, and (ii) zero initial slip velocity. For further clarification, Fig. 13 presents the MSD computed over 10^4 particle trajectories, initially distributed within the basic vortex cell with zero initial slip velocity, for a few representative cases of St and R as a function of time. All MSD curves asymptotically follow a t^2 scaling at long times, confirming the presence of longtime ballistic motion. For verification, we also generated a contour plot of the exponent n, as in Fig. 10(a), but incorporating history effects. However, the plot is not included here, as it displayed a uniform color, indicating that the numerically computed n values were close to 2 for all cases, with slight deviations. We attribute these deviations to the finite simulation time, which was restricted to $t = 10^4$. If the simulations were extended to much larger times, then we expect that n would asymptotically approach 2. From Fig. 13, it can also be seen that while the MSD asymptotically approaches a ballistic regime at long times, some parametric cases exhibit transient trapped behavior at intermediate times (e.g., see the

blue curve). This shows a residual influence of the dynamics observed in the absence of the history force.

It is interesting to observe that the inclusion of history force into the dynamics eliminates the presence of trapped and diffusive dynamical states, resulting in a transition to a ballistic state at longtime across all parametric conditions examined in this study. To comprehend this behavior, we analyze particle motion in the limit of $\mathrm{St} \ll R$, expressing particle velocity as the sum of fluid velocity and its higher-order derivatives up to $\mathcal{O}(\mathrm{St}^{3/2})$, thereby accounting for the effects of history force as proposed by Ferry and Balachandar [15]. We identify the history along the particle trajectory by integrating the particle velocity at the leading orders initialized near the separatrix. As particles approach the stagnation point, the history force directs out of the vortex cell, facilitating particle intercell jumping, which is consistent with the earlier findings of Druzhinin and Ostrovsky [30]. As the particle reaches the next stagnation point following the initial jump, the components of its history reverse their signs while still maintaining their outward direction from the cell. This alternating sign change in the history force leads the particle to exhibit a zigzag motion, resulting in ballistic movement over a long time. For further details, readers may refer to Appendix E. While a complete understanding remains open, our results suggest that the history force suppresses particle trapping near separatrices (as discussed in Sec. III C), thereby allowing particles to leak more easily across successive vortex cells. This leads to open trajectories and the disappearance of limit cycles or confined motion. The system is inherently sensitive, so even small perturbations introduced by the history term can result in large changes in trajectories, particularly near stagnation zones, as illustrated in Fig. 12. However, the diffusive trajectories—typically associated with chaotic intercell transitions—being completely absent is less straightforward to interpret and may point to an unexpectedly coherent transport mechanism driven by the history term. A more thorough investigation into this transition remains an intriguing direction for future work.

This study is dedicated to highlighting the effects of the history force on particle dynamics and how they differ from cases where only inertial forces (pressure gradient and added mass effects) are considered along with Stokes drag. However, the earlier sections mainly focus on particle dynamics in the absence of the history force, as these cases are also relevant in certain physical scenarios and cannot simply be dismissed as oversimplified approximations. In our analysis, we have employed a specific form of the history force corresponding to the Boussinesq-Basset history kernel, which decays as $\mathcal{O}(t^{-1/2})$ with time. Our findings indicate that this force significantly influences particle dynamics. In particular, it allows particles to cross flow separatrices even at low St, R, in finite time. Furthermore, at asymptotically long times, the presence of this history force results in ballistic transport for all particles, irrespective of values of St, R, or initial conditions. However, these modifications due to the history force must be interpreted with caution. The Boussinesq-Basset kernel is valid in the limit of $\mathrm{Re} = 0$. For any finite but small Reynolds number ($\mathrm{Re} \ll 1$), more appropriate history kernels exist [50–52], which exhibit a much faster decay, such as $\mathcal{O}(t^{-2})$. If such kernels were used, then the longtime ballistic behavior observed in this section would not be an accurate representation of the true dynamics. Instead, at sufficiently long times, the influence of the history force would diminish relative to other inertial forces, making the dynamical behaviors described in the previous sections (Secs. III A, III B, and IV, where the history force was neglected purposely) more appropriate. Nevertheless, for short times, the history force remains relevant and should not be excluded from consideration.

VI. SUMMARY AND CONCLUSIONS

We investigated the dynamics of inertial particles that are heavier than the fluid in a 2D steady TG vortex flow, characterized by an infinite array of vortices. Tracers remain confined within the vortical cells, following the closed streamlines of the flow. Conversely, finitely heavier inertial particles with $\mathrm{St} \neq 0$ and $R > 2/3$ exhibit the potential to cross streamlines and traverse through these vortical structures, depending on the specific values of St and R. Previous studies [24,25,34] have reported that under the infinitely heavy particle limit, where $R = 1$, inertial particles remain trapped within

a vortex cell if the Stokes number satisfies the condition $\mathrm{St} < \mathrm{St}_c = 1/4$, assuming that the impacts of inertial and history forces are negligible.

We derived a general expression for the critical Stokes number St_c by employing linear stability analysis to examine particle dynamics in the vicinity of corner fixed points (stagnation points) of TG vortex flow. We categorized the distinct regions of dynamical behavior on the St-R parameter plane based on the characteristics of the eigenvalues. In region A, situated below the critical Stokes number line St_c^+, particles exhibited nonoscillatory trajectories as the fixed points showed 3:1 saddle features. As a result, the particles are restricted from moving across the flow separatrices, leading to their confinement. Notably, this trapping dynamics remained consistent irrespective of whether the particles were initialized with zero velocity or zero slip. In region B, bounded by the curves St_c^+ and St_c^-, the nature of the saddle fixed points transition to a spiral-3:1 saddle configuration. Here, the oscillatory nature of particle trajectories allows particles to move across the flow separatrices and lead them to neighboring vortex cells. Region C, delineated by St_c^- and St_{c_p}, shared similarities in fixed point features with region A. Finally, the region D, located beyond St_{c_p}, was characterized by particle trajectories that will not align with separatrix axes at the long time limit. Here, the fixed point has a 2:2 saddle nature in the phase space. Even though the particle trajectories do not have an oscillatory nature in regions A, C, and D, appropriate initial velocity/momentum can make them cross the flow separatrices as described in Appendix C. At large values of Stokes number, we presented an analysis regarding the emergence of additional fixed points in the flow field, attributing these to the influence of inertial forces (added mass and pressure gradient forces). We linearized the flow field in proximity to these edge fixed points, and also analyzed the corresponding dynamics of the particles, as well as the trajectory equations. Notably, these newly identified fixed points only exist in the region D of the parametric space. We also examined the eigenvalue characteristics to delineate region D into two subregions: D_1, where these edge fixed points exhibited 3:1 saddle behavior alongside already existing corner fixed points which are 2:2 saddles; and D_2, where the behavior of the edge fixed points transitioned to a spiral-3:1 saddle nature, while the corner fixed points remained as 2:2 saddles.

In the absence of a history force, the critical time t_{cr} required for the particles to first cross the separatrix axis the flow field exhibits a singular scaling $(\mathrm{St} - \mathrm{St}_c)^{-1/2}$ as the Stokes number approached the critical value St_c for a given density parameter R. Conversely, in the presence of a history force, the t_{cr} curve demonstrated a smooth variation with St, indicating that particles are able to cross the separatrix lines, irrespective of the values of St and R, provided they are initialized with zero slip velocity. For zero initial velocity of the particles, we also expect qualitatively the same behavior to exist. We have also found that particles with lower St and R values required a longer duration to cross the extensional axis, whereas particles with higher St and R values required comparatively less time for crossing the separatrix line.

We numerically investigated particle dynamics in the fully nonlinear TG vortex flow, focusing particularly on longtime dispersion behavior, which we quantified using MSD. We identified and delineated parameter regimes in the St-R plane, where trapped, diffusive, and ballistic particle dynamics emerged at the long time limit. Our analysis revealed two distinct trapped regions in the parameter space: the first corresponded to particles remaining confined within their initial vortex cell, the same as the trapping zone observed in the linearized flow cases, while the second corresponded to particles becoming trapped in a different vortex cell after crossing the initial one.

For a given parametric combination of St and R, we tracked individual particle trajectories and identified their dynamical nature based on the scaling of their single-particle squared displacement with time. This scaling gave us insight into individual particle dispersion behavior, going beyond the mean trend indicated by the MSD. Our analysis revealed that while the MSD reflected the dominant behavior of particles initialized within the vortex cell, not all particles exhibited the same dynamics. Even when the MSD indicated ballistic behavior, a fraction of particles displayed subdominant diffusive or trapped dispersion. Accordingly, we quantified and reported the fractions of particles demonstrating ballistic, diffusive, and trapped behavior. This observation aligned with a previous study by Nath *et al.* [24] for infinitely heavy particles.

In the presence of the history force, our investigation identified modifications to particle dynamics in the nonlinear TG vortex flow. We concentrated our analysis on the restricted parameter regime: St $\in (0.1, 1)$ and $R \in (2/3, 1)$. The introduction of the history force led to the disappearance of the previously identified trapped and diffusive regions in the St-R parametric space. Notably, even particles with low values of St and R were able to escape their initial vortex cells without becoming trapped anywhere. At long times, we observed that the MSD, as well as the single-particle SD of individual particles, became indistinguishable, both exhibiting a quadratic scaling with time. This behavior signifies that all particles show ballistic dispersion, irrespective of variations in St, R, or their initial positions.

To conclude, we have systematically explored the dynamics of inertial particles in a two-dimensional steady Taylor-Green vortex flow, focusing on analyzing the roles of hydrodynamic forces such as added mass, pressure gradient, and history forces. By employing linear stability analysis and nonlinear simulations, we have mapped out the parametric regimes in St-R plane that govern particle trapping, separatrix crossing, and long-term dispersion behaviors. Our results identified that, in the absence of the history force, particle motion is highly sensitive to particle inertia, density ratio, and initial conditions, leading to a wide variety of dynamical regimes, including trapping, diffusive, and ballistic transport. Remarkably, the inclusion of the history force erases these boundaries, universally promoting ballistic motion regardless of particle parameters or initial locations. These insights advance our fundamental understanding of inertial particle transport in structured flows and offer predictive tools for a wide range of applications in environmental and engineering contexts.

While our study provides a detailed characterization of inertial particle dynamics in a steady TG vortex flow, several limitations and open questions remain. First, the analysis is confined to idealized, two-dimensional, and steady flow conditions; real-world flows are often three-dimensional, time-dependent, and may involve turbulence or additional forces such as gravity and Brownian motion. For instance, a recent report by Kumar *et al.* [53] emphasizes the impact of unsteadiness on particle dynamics, showing that periodic switching of stagnation points and vortices can lead to chaotic particle trajectories, even for tracer particles. Furthermore, the sensitivity of particle trajectories to initial conditions and the inherently nonergodic nature of their transport imply that even small perturbations—arising from turbulence, boundaries, or particle–particle interactions—could significantly influence the dynamics. Although we find that the history force facilitates particle crossing of flow separatrices and promotes ballistic dispersion, its influence may vary if a different kernel is used. Future research could extend our framework to unsteady or turbulent flows, investigate the role of finite particle sizes and shapes, incorporate stochastic forcing, or examine the consequences of symmetry breaking in the flow field. Such efforts would not only test the generality of our findings but also help bridge the gap between idealized theoretical models and complex real-world systems.

ACKNOWLEDGMENTS

P.K. acknowledges insightful discussions with Divya Jaganathan on the integration of the history force, which contributed to the refinement of this work. A.V.S.N. acknowledges support from the Prime Minister's Research Fellows (PMRF) scheme, Ministry of Education, Government of India (IN).

DATA AVAILABILITY

No data were created or analyzed in this study.

APPENDIX A: KINEMATICS OF THE MODIFIED FLOW

In this Appendix, we analyze the kinematic equations governing the modified flow field perceived by inertial particles in a TG vortex. We derive the stability and nature of fixed points through

linearization and eigenvalue analysis, elucidating their role in shaping streamline topology. The effective flow field, incorporating inertial forces (added mass and pressure gradient), is described by

$$\dot{x} = \sin x\,(\cos y + \gamma^{-1}\cos x), \tag{A1a}$$

$$\dot{y} = \sin y\,(-\cos x + \gamma^{-1}\cos y), \tag{A1b}$$

where $\dot{x}$ and $\dot{y}$ represent the velocities of tracers along the x and y directions, respectively, and $\gamma = \mathrm{St}_{c_p}/\mathrm{St}$ is a parameter defined in Sec. III. Unlike the classical incompressible TG vortex–in Eq. (4), this modified flow is compressible, which fundamentally alters the nature of the fixed points and corresponding flow kinematics. To understand the local behavior near these fixed points, we perform a linearization of the governing equations.

A formal linearization of Eq. (A1) near a CFP, say $(0,\ 0)$, yields the following:

$$\begin{bmatrix}\dot{x}\\ \dot{y}\end{bmatrix} = \begin{bmatrix}1+\gamma^{-1} & 0\\ 0 & -1+\gamma^{-1}\end{bmatrix}\begin{bmatrix}x\\ y\end{bmatrix}. \tag{A2}$$

The eigenvalues of the linearized Eq. (A2) are given by

$$\lambda^{\pm}_{k_c} = \gamma^{-1} \pm 1. \tag{A3}$$

Based on the eigenvalue $\lambda^{\pm}_{k_c}$ characteristics, the corner fixed point indicates a saddle-type behavior when $\gamma^{-1} < 1$ or $(\mathrm{St} < \mathrm{St}_{c_p})$, recall γ is defined as $\mathrm{St}_{c_p}/\mathrm{St}$ in Sec. III. The behavior transition to source-type when $\gamma^{-1} > 1$ or $(\mathrm{St} > \mathrm{St}_{c_p})$. The source-type behavior of corner fixed points is possible here because of the compressible nature of the effective flow field. As discussed in Sec. III, when $\mathrm{St} > \mathrm{St}_{c_p}$, the EFPs emerge. Linearizing the kinematic equations [Eqs. (A1)] about a EFP, say $(\cos^{-1}[-\gamma],\ 0)$ yields the following:

$$\begin{bmatrix}\dot{x}\\ \dot{y}\end{bmatrix} = \begin{bmatrix}\gamma-\gamma^{-1} & 0\\ 0 & \gamma+\gamma^{-1}\end{bmatrix}\begin{bmatrix}x\\ y\end{bmatrix}. \tag{A4}$$

We get the following eigenvalues corresponding to Eqs. (A4)

$$\lambda^{\pm}_{k_n} = \gamma \pm \gamma^{-1}. \tag{A5}$$

Hence, the edge fixed points exhibit a saddle-type behavior. The linearized equations near to the cell center $(\pi/2,\ \pi/2)$ are as follows:

$$\begin{bmatrix}\dot{x}\\ \dot{y}\end{bmatrix} = \begin{bmatrix}-\gamma^{-1} & -1\\ 1 & -\gamma^{-1}\end{bmatrix}\begin{bmatrix}x\\ y\end{bmatrix}. \tag{A6}$$

The eigenvalues associated with Eqs. (A6) are as follows:

$$\lambda^{\pm}_{k_s} = -\gamma^{-1} \pm i. \tag{A7}$$

The eigenvalue $\lambda^{\pm}_{k_s}$ signify a spiral attractor behavior of cell center when $\gamma^{-1} \neq 0$. It is important to note that these eigenvalues and the associated fixed point classifications describe the nature of streamlines in the effective flow field near their vicinity, which aligns well with the examples in Fig. 2.

APPENDIX B: PARTICLE DYNAMICS NEAR A CENTER FIXED POINT OF TG VORTEX FLOW

In this Appendix, we analyze the particle dynamics in the vicinity of the cell center of TG vortex flows. The flow field near the center fixed point, located at, say, $(\pi/2,\ \pi/2)$, closely approximates a solid-body rotation. To leading order, the velocity components can be expressed as

$$u_x \approx -y, \tag{B1a}$$

$$u_y \approx x, \tag{B1b}$$

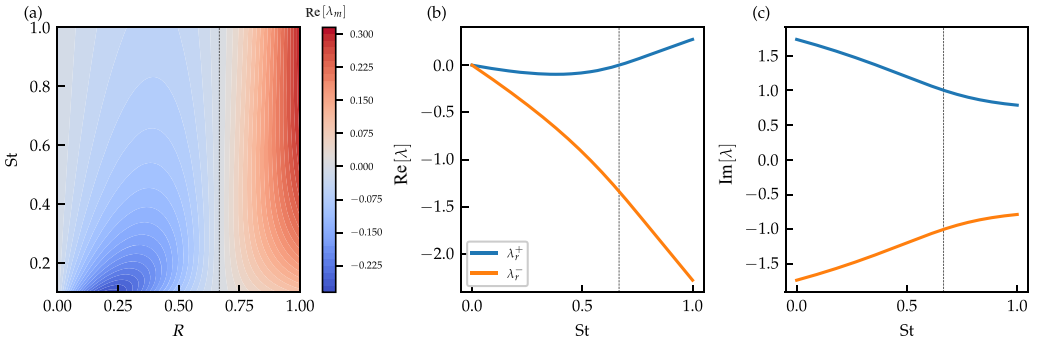

FIG. 14. (a) Contour plot of the real part eigenvalue with the highest real part (λ_m) in the St-R parametric plane. The evolution of (b) real and (c) imaginary parts of eigenvalues at St $= 0.5$ with R. The dark dotted lines represent $R = 2/3$, above which particles are heavier than the fluid.

which describes a counterclockwise rotational flow about the cell center. Adopting a dynamical systems approach, we first analyze the effects of Stokes drag and inertial forces while excluding the history force. Subsequently, we incorporate the history force to examine its influence on the particle dynamics.

1. Without history force

In the vicinity of the cell center, and excluding the history force, the governing equations [Eq. (5)] reduce to

$$\frac{1}{R}\ddot{x} + \frac{1}{\mathrm{St}}\dot{x} + \frac{3(1-R)}{R}x + \frac{1}{\mathrm{St}}y = 0, \tag{B2a}$$

$$\frac{1}{R}\ddot{y} + \frac{1}{\mathrm{St}}\dot{y} + \frac{3(1-R)}{R}y - \frac{1}{\mathrm{St}}x = 0. \tag{B2b}$$

Unlike Eqs. (12), which remain decoupled, Eqs. (B2) form a set of coupled second-order differential equations. Introducing a complex variable $z = x + i\,y$, where $i^2 = -1$, we can combine Eqs. (B2) into the following single complex equation:

$$\frac{1}{R}\ddot{z} + \frac{1}{\mathrm{St}}\dot{z} + \left[\frac{3(1-R)}{R} - \frac{1}{\mathrm{St}}\,i\right]z = 0. \tag{B3}$$

We express the solution for z as

$$z = C_{r1}\exp(\lambda_r^+\,t) + C_{r2}\exp(\lambda_r^-\,t) \quad \text{with} \quad \lambda_r^{\pm} = \frac{1}{2}\left(-\frac{R}{\mathrm{St}} \pm \sqrt{\left(\frac{R}{\mathrm{St}}\right)^2 + \frac{4R}{\mathrm{St}}i + 12(R-1)}\right), \tag{B4}$$

where C_{r1} and C_{r1} are the integration constants which depend on initial conditions ($Z_0 = X_0 + i\,Y_0,\ \dot{z}_0 = \dot{x}_0 + i\,\dot{y}_0$) and the eigenvalues ($\lambda_r^{\pm}$). We determine them as

$$C_{r_1} = \frac{Z_0\lambda_r^- - \dot{z}_0}{\lambda_r^- - \lambda_r^+},\ C_{r_2} = \frac{\dot{z}_0 - Z_0\lambda_r^+}{\lambda_r^- - \lambda_r^+}. \tag{B5}$$

Note that the eigenvalues ($\lambda_r^{\pm}$) are inherently complex, which signifies oscillatory or spiralling particle trajectories in the vicinity of the center fixed point. To further elucidate the local behavior of particle dynamics near the vortex center of TG vortex flows, we present the contour of the real part of the dominant eigenvalue, denoted as λ_m, in Fig. 14(a). As illustrated in Fig. 14(a), the real

part of λ_m is positive for $R > 2/3$, indicating that heavier particles are centrifuged outward from the vortex center. In contrast, lighter particles asymptotically approach the vortex center due to the negative real part of λ_m. To characterize this transition more clearly, we plot the variation of the real and imaginary parts of the eigenvalues with respect to R at a fixed $\mathrm{St} = 0.50$ in Figs. 14(b) and 14(c). These plots identify a transition in the sign of the real part at $R = 2/3$, while the imaginary parts remain nonzero throughout, signifying a shift in the dynamics from a spiral sink to a spiral source.

2. With history force

When we account for the effects of the history force, the governing equations [Eqs. (5)] in the vicinity of the cell center simplify to

$$\ddot{x} + \frac{R}{\mathrm{St}}\dot{x} + 3(1-\mathrm{R})\,x + \frac{R}{\mathrm{St}}\,y = -\frac{\kappa}{\sqrt{\pi}}\left[\frac{\dot{x}_0 + y_0}{\sqrt{t}} + \int_0^t \frac{1}{\sqrt{t-t'}}(\ddot{x} + \dot{y})dt'\right], \tag{B6a}$$

$$\ddot{y} + \frac{R}{\mathrm{St}}\dot{y} + 3(1-R)\,y - \frac{R}{\mathrm{St}}\,x = -\frac{\kappa}{\sqrt{\pi}}\left[\frac{\dot{y}_0 - x_0}{\sqrt{t}} + \int_0^t \frac{1}{\sqrt{t-t'}}(\ddot{y} - \dot{x})dt'\right]. \tag{B6b}$$

As before, we observe that Eqs. (B6a) and (B6b) form a coupled system. To simplify the analysis, we introduce the complex variable $z = x + i\,y$ and recast the equations as follows:

$$\ddot{z} + \frac{R}{\mathrm{St}}\dot{z} + \left\{3(1-R) - \frac{R}{\mathrm{St}}\,i\right\} z = -\frac{\kappa}{\sqrt{\pi}}\left[\frac{\dot{z}_0 - z_0\,i}{\sqrt{t}} + \int_0^t \frac{1}{\sqrt{t-t'}}(\ddot{z} - \dot{z}\,i)dt'\right]. \tag{B7}$$

Similar to the analysis in Sec. III C, we apply the Laplace transform to Eq. (B7), converting it into the Laplace domain as follows:

$$\hat{z} = \frac{1}{\prod_{i=1}^{4}\sqrt{s} - \mu_{z_i}}\left(s\,z_0 + \sqrt{s}\,\kappa\,z_0 + \frac{R}{\mathrm{St}}z_0 + \dot{z}_0\right). \tag{B8}$$

Here, $\hat{z}$ denotes the variable in the Laplace domain, corresponding to z in the physical domain. The terms μ_{z_i} represent the roots of the quartic polynomial, $p_z(\zeta) = \zeta^4 + \kappa\,\zeta^3 + (R/\mathrm{St})\,\zeta^2 - \kappa\,i\,\zeta + [3(1-R) - (R/\mathrm{St})\,i]$. We obtain the general solution for the particle trajectory $z(t)$ in the complex plane by performing partial fraction decomposition followed by the inverse Laplace transform on Eq. (B8):

$$z(t) = \Sigma_{i=1}^{4} A_{z_i}\mu_{z_i}\exp\left(\mu_{z_i}^2\,t\right)\mathrm{erfc}(-\mu_{z_i}\sqrt{t}). \tag{B9}$$

The coefficient A_{z_i} is given by

$$A_{z_i} = \frac{z_0\left(\mu_{Z_i}^2 + \kappa\,\mu_{z_i}\right) + \frac{R}{\mathrm{St}}z_0 + \dot{z}_0}{\prod_{j\neq i,\ j=i}^{j=4}\left(\mu_{z_i} - \mu_{z_j}\right)} \quad \Sigma_{i=1}^{4} A_{z_i} = 0. \tag{B10}$$

The coefficient A_{z_i} depends on the parameters (St and R), the initial conditions, and the corresponding root μ_{z_i}.

To analyze the influence of the history force on particle dynamics, we compare analytically computed typical particle trajectories with and without the history force. Particles are initialized at $(x = 0.01,\ 0.01)$ with zero slip velocity, using parameters $(R = 0.4,\ \mathrm{St} = 0.1)$ for light particles and $(R = 0.8,\ \mathrm{St} = 0.1)$ for heavy particles. For the light particle case, we observe that particles asymptotically approach the cell center in both scenarios. However, the rate of approach is significantly reduced when the history force is considered, as shown in Fig. 15(a). However, heavy particles move away from the cell center in both the presence and absence of the history force. However, in the presence of history force, their outward migration occurs at a slower rate, as shown in Fig. 15(b). These results align with the earlier work of Candelier *et al.* [31]. They investigated the effects of the history force in solid-body rotational flows using experimental observations and theoretical analysis.

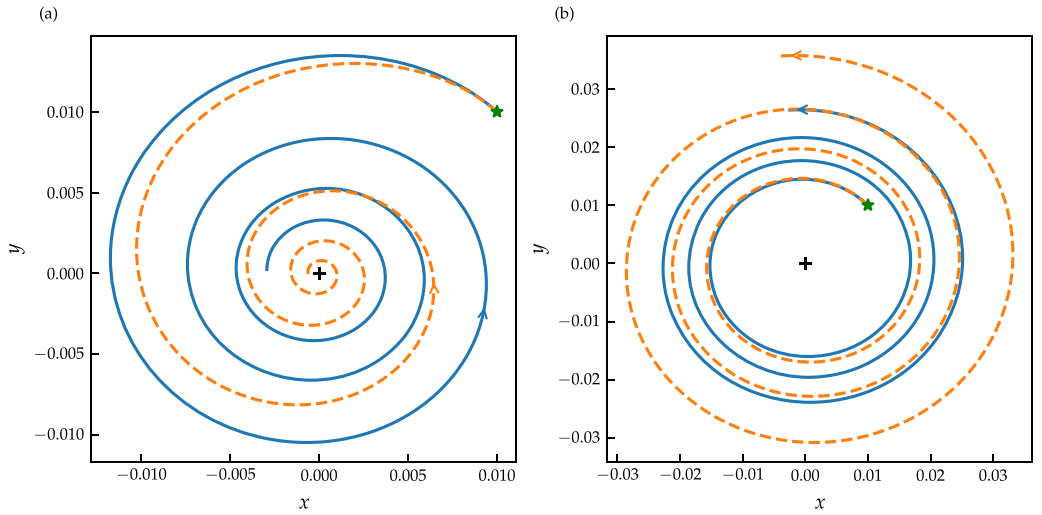

FIG. 15. Particle trajectories computed without (dashed line) and with (solid line) the history force for (a) a light particle ($R = 0.4,\ \mathrm{St} = 0.1$) and (b) a heavy particle ($R = 0.8,\ \mathrm{St} = 0.1$). In both scenarios, particles are initialized at ($x = 0.01,\ y = 0.01$), indicated with a star ($*$) symbol, with zero slip velocity. Symbol $+$ indicates the location of the cell center.

APPENDIX C: EFFECTS OF INITIAL CONDITIONS ON SEPARATRIX CROSSING

The integration constants C_1, C_2, C_3, and C_4 corresponding to Eq. (13) depends on the initial conditions as follows:

$$C_1 = \frac{v_{x_0} - x_0\,\lambda_e^-}{\lambda_e^+ - \lambda_e^-},\ C_2 = \frac{-v_{x_0} + x_0\,\lambda_e^+}{\lambda_e^+ - \lambda_e^-},\ C_3 = \frac{v_{y_0} - y_0\,\lambda_c^-}{\lambda_c^+ - \lambda_c^-},\ \text{and}\ C_4 = \frac{-v_{y_0} + y_0\,\lambda_c^+}{\lambda_c^+ - \lambda_c^-}, \tag{C1}$$

where $x(t=0) = x_0$, $y(t=0) = y_0$, $v_x(t=0) = v_{x_0}$, and $v_y(t=0) = v_{y_0}$. Let us first focus on the special case discussed in Sec. III A, where particles can cross extensional separatrix even when their trajectories are nonoscillatory—as seen in regions A, C, and D—provided that suitable initial conditions are satisfied. Intuitively, one may expect that an inertial particle needs sufficient momentum in the direction normal to a barrier to cross it. The same principle applies here: crossing the separatrix requires adequate initial momentum oriented across the extensional axis. Although the solution in Eq. (13b) is nonoscillatory when both eigenvalues λ_c^+ and λ_c^- are real, it is still possible for the particle trajectory to reach $y = 0$ line at a finite time—implying a potential crossing of the extensional axis. The condition for such a crossing can be obtained by solving for $y = 0$ using Eq. (13b), which gives the first crossing time as

$$t_{\mathrm{cr}} = \frac{\ln(-C_4/C_3)}{(\lambda_c^+ - \lambda_c^-)} = \frac{2\,\mathrm{St}}{\sqrt{R^2 - 4R\,\mathrm{St} + 12\,(1-R)\,\mathrm{St}^2}} \times \tanh^{-1}\left[-\frac{\sqrt{R^2 - 4R\,\mathrm{St} + 12\,(1-R)\,\mathrm{St}^2}}{R + 2\,\mathrm{St}\,\frac{v_{y_0}}{y_0}}\right]. \tag{C2}$$

For t_{cr} to be real, positive, and finite, the following conditions must be satisfied: When both λ_c^+ and λ_c^- are real, the particle trajectory can cross the extensional separatrix axis only if (i) for $y_0 > 0$, the initial velocity satisfies $v_{y_0} < y_0\,\lambda_c^-$, and (ii) for $y_0 < 0$, it satisfies $v_{y_0} > y_0\,\lambda_c^-$. That is, for particles in regions A, C, and D to cross the extensional separatrix (which is y = 0 when considering the CFP near the origin, without loss of generality), the component of the initial velocity normal to the axis (here v_{y_0}) must meet the above criteria. Note that if the extensional axis is instead aligned

along $x = 0$, the same condition and the expression for t_{cr} in equation (C2) still apply, with the substitutions $y_0 \to x_0$ and $v_{y_0} \to v_{x_0}$.

In region B, however, the eigenvalues $\lambda_c^{\pm}$ form a complex conjugate pair, leading to oscillatory particle trajectories about the extensional axis. As a result, particles are expected to cross the extensional separatrix regardless of their initial conditions. This is evident from the expression for the first crossing time, appropriately modified from Eq. (C2), given as

$$t_{cr} = \frac{2\,\mathrm{St}}{\sqrt{-R^2 + 4\,R\,\mathrm{St} - 12\,(1-R)\,\mathrm{St}^2}} \left\{ \pi - \tan^{-1}\left[\frac{\sqrt{-R^2 + 4\,R\,\mathrm{St} - 12\,(1-R)\,\mathrm{St}^2}}{R + 2\,\mathrm{St}\,\frac{v_{y_0}}{y_0}} \right] \right\}. \quad \text{(C3)}$$

Note that, irrespective of the values of y_0 or v_{y_0}, the crossing time t_{cr} can still be a real, positive quantity, implying that the particle can cross the extensional separatrix within a finite time.

In a similar manner, particle trajectories can also cross the compressional separatrix line (here, $x = 0$) under suitable initial conditions. Since the eigenvalues λ_e^+ and λ_e^- are real across all regions A, B, C, and D, crossing the compressional separatrix axis is only possible through appropriate initial conditions only—unlike in region B, where oscillatory trajectories enable extensional axis crossing. Applying the same approach as before, but now using Eq. (13a), one can determine the conditions under which $x = 0$ is reached at a real, finite time. This yields an expression for the first crossing time analogous to Eq. (C2), given as

$$t_{cr} = \frac{\ln(-C_2/C_1)}{(\lambda_e^+ - \lambda_e^-)} = \frac{2\,\mathrm{St}}{\sqrt{R^2 + 4\,R\,\mathrm{St} + 12\,(1-R)\,\mathrm{St}^2}} \tanh^{-1}\left[-\frac{\sqrt{R^2 + 4\,R\,\mathrm{St} + 12\,(1-R)\,\mathrm{St}^2}}{R + 2\,\mathrm{St}\,\frac{v_{x_0}}{x_0}} \right]. \quad \text{(C4)}$$

Accordingly, the criterion for crossing the compressional separatrix (here, $x = 0$) becomes: the particle trajectory can intersect this axis only if (i) for $x_0 > 0$, the initial velocity satisfy $v_{x_0} < x_0\,\lambda_e^-$; and (ii) for $x_0 < 0$, the condition is $v_{x_0} > x_0\,\lambda_e^-$. As mentioned earlier, this condition, along with expression (C4), applies not only to regions A, C, and D, but also to region B, as the trajectories are not oscillatory here. If the compressional separatrix is instead is $y = 0$ line, then the same expression and conditions remain valid upon substituting x_0 with y_0, and v_{x_0} with v_{y_0}.

APPENDIX D: TRAPPING OF ESCAPED PARTICLES IN DISTANT VORTEX CELLS

In Sec. IV, we observed that particles that escape from their initial vortex cell can later become trapped in a distant vortex cell. This behavior is characteristic of the parameter regime identified as region IIIa in Fig. 10(a). Notably, this region lies within region B in Fig. 4(a), where the corresponding CFPs are spiral 3:1 saddles. As a result, particle trajectories in this regime exhibit oscillatory behavior and can, in principle, cross separatrices regardless of their momentum near the fixed points as per the findings in Appendix C. However, despite their ability to cross the separatrices and escape their initial vortex cell, particles in region IIIa often become confined after traversing a few neighboring cells. In contrast, particles in region II—also part of the region B—do not exhibit such confinement and continue to migrate unboundedly across multiple vortex cells. In this Appendix, we aim to investigate and explain the reason behind this selective trapping behavior observed in region IIIa.

The key difference we identified in region IIIa is that, although particles escape their initial vortex cell, their closest distance from the CFPs of subsequent cells tends to decrease over time—suggesting a gradual loss of kinetic energy. Eventually, in a distant cell, the particle passes extremely close to its CFP, significantly closer than it ever was in the initial cell. Once this distance falls below the numerical precision threshold (typically around 10^{-14}), the particle is effectively treated as having reached the fixed point and is numerically considered trapped. In contrast, particles in region II display a different behavior. Each time they traverse near a CFP, they tend to gain kinetic energy, allowing them to move farther from the CFP in the next cell. Although this distance

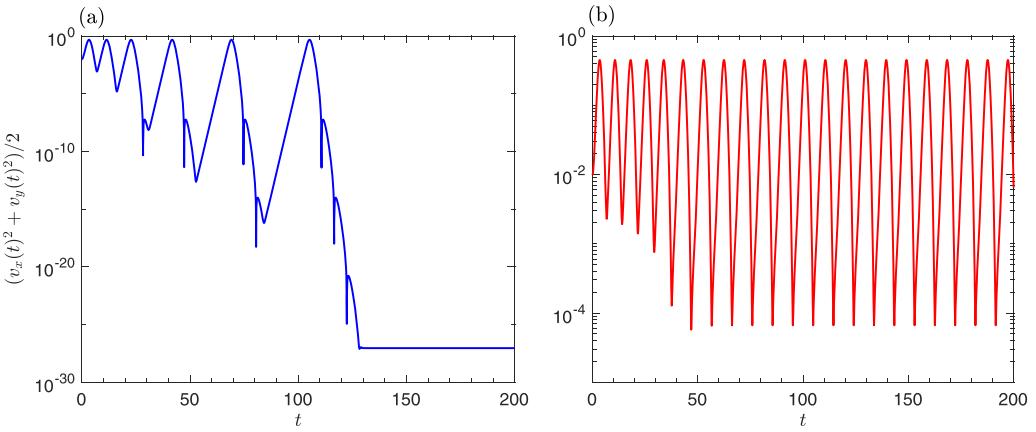

FIG. 16. The kinetic energy, given by $(v_x(t)^2 + v_y(t)^2)/2$, is plotted against time for representative particle trajectories in regions IIIa and II, shown in panels (a) and (b), respectively. Particles are initialized within the basic vortex cell at $(x, y) = (0.1, 0.1)$ with zero initial slip velocity. The parameters used are: (a) St $= 0.3$, $R = 0.8$; and (b) St $= 0.5$, $R = 0.8$.

eventually saturates, it remains sufficient to avoid numerical trapping. As a result, these particles continue along open trajectories across multiple vortex cells without confinement. Whether such trajectories are ultimately ballistic or diffusive is a separate question, beyond the scope of the current discussion. To illustrate this distinction, we plot the evolution of the kinetic energy, computed as $(v_x(t)^2 + v_y(t)^2)/2$, for representative particle trajectories from regions IIIa and II in Fig. 16. As shown in Fig. 16(a), the kinetic energy of a particle in region IIIa exhibits an oscillatory pattern. The kinetic energy peaks when the particle is escaping from a CFP and dips when it approaches the CFP, where it slows down. While the maximum values remain of order unity, the minimum values decrease progressively with each cycle, eventually reaching magnitudes as low as 10^{-28}. This corresponds to particle velocities and distances from the fixed point on the order of 10^{-14}, below the numerical precision threshold, and is thus effectively treated as zero. As a result, the particle is considered to have been captured by the corresponding CFP. In contrast, for a particle in region II, as shown in Fig. 16(b), the kinetic energy also oscillates, with peak values remaining of order unity. However, while the minima initially decrease, they eventually saturate at a finite value. This indicates that the particle retains sufficient energy to continue its motion indefinitely, traversing multiple vortex cells without becoming trapped.

The remaining task is to derive a critical criterion that can predict whether a particle will eventually become trapped or continue escaping through multiple vortex cells. For this, we consider the schematic representations in Fig. 17, which illustrate typical oscillatory trajectory segments of a particle in a TG vortex cell. In Fig. 17(a), the particle reaches near the CFP located at the bottom-left corner, with an initial velocity approximately vertical, i.e., v_{y_0} is finite while $v_{x_0} \approx 0$, and it is horizontally offset from the CFP by the positive distance x_0. The trajectory then evolves along a path that stays close to the extensional separatrix line (though exaggerated here for visibility), reaching near the bottom-right CFP with an almost horizontal velocity v_{x_1} (i.e., $v_{y_1} \approx 0$), and a vertical offset of positive value y_1 from the CFP. A similar sequence occurs in Fig. 17(b), with the primary distinction being that the particle arrives at the next CFP with a negative offset, i.e., $y_1 < 0$, due to an extra/less oscillation in the trajectory. Once the particle reaches this point, its subsequent motion may be viewed as starting from y_1 with velocity v_{x_1}, and evolving along the compressional separatrix—essentially repeating a topologically similar trajectory segment with the roles of the x and y axes interchanged. This process continues iteratively across successive vortex cells. Our objective is to determine whether the particle's separation from the nearest CFP decreases

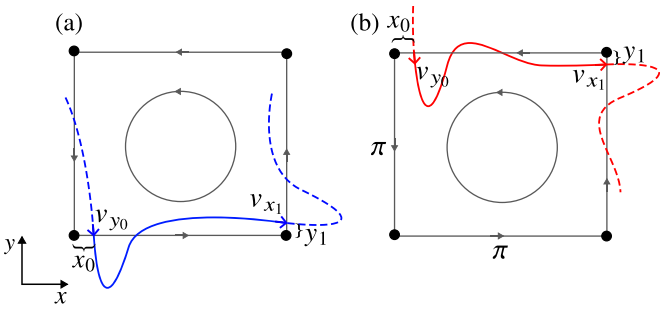

FIG. 17. The schematic illustrates typical trajectory segments of particles in region B as they traverse near CFPs. The solid (undashed) portion of the trajectory continues qualitatively beyond the shown segment (as dashed parts), with the roles of the extensional and compressional axes interchanged. As in (a), if the segment exhibits an even number of zero crossings, then it terminates at a positive distance from the CFP, indicating the possibility of a closed trajectory. As in (b), an odd number of zero crossings causes the segment to end at a negative distance from the CFP, suggesting the likelihood of an open trajectory.

or increases after each such segment. That is, we examine whether $|y_1|$ is less than or greater than x_0. If $|y_1| < x_0$, then the particle's kinetic energy diminishes after each passage near a CFP, eventually reducing its distance from the CFP below the numerical precision threshold and causing it to be interpreted as captured. Conversely, if $|y_1| > x_0$, then the particle retains sufficient energy to avoid being trapped and continues its motion across multiple cells.

To determine this criterion precisely, we consider solving the system of equations (7) with the initial conditions: $x(t=0) = x_0$, $v_x(t=0) = 0$, $y(t=0) = 0$ and $v_y(t=0) = v_{y_0}$, for some finite values of x_0 and v_{y_0}. Here we choose $x_0 > 0$ and $v_{y_0} < 0$ without loss of generality. Note that x_0 can be chosen as an arbitrarily small positive quantity in theory without affecting the qualitative dynamics. The integration is carried out until a time t_1, defined such that $x(t=t_1) = \pi$, and the corresponding vertical separation is $y(t=t_1) = y_1$ from the nearest CFP. The key diagnostic quantity is then the ratio $|y_1|/x_0$, and whether it is less than or greater than unity determines the outcome. Particularly, under what conditions on the parameters and initializations does the ratio $|y_1|/x_0$ exactly equal one? This would represent the critical condition separating confined and unbounded particle dynamics. However, since the system (7) is nonlinear, obtaining an analytical solution is generally infeasible, and we must rely on numerical integration. To make analytical progress and derive an approximate criterion, we propose to linearize the system under specific assumptions. In the following, we introduce a two-level approximation strategy to achieve this.

First, observe that for sufficiently small values of x_0 and v_{y_0}, the resulting trajectory segment remains close to the extensional separatrix axis. In this regime, the vertical displacement remains small throughout the motion, i.e., $|y(t)| \ll 1$. This observation allows us to apply a first-level approximation to equations (7), where we linearize the trigonometric functions as $\sin y \approx y$, and $\cos y \approx 1$. Substituting these approximations into the governing equations yields a weakly nonlinear system of the form as

$$\ddot{x} = -\frac{R}{\mathrm{St}}\left(\dot{x} - \sin x\right) + 3\left(1 - R\right)\,\sin x\,\cos x, \tag{D1a}$$

$$\ddot{y} = -\frac{R}{\mathrm{St}}\left(\dot{y} + y\,\cos x\right) + 3\left(1 - R\right)y. \tag{D1b}$$

Note that despite the linearization in y, the system remains nonlinear in x, as $x(t)$ spans a relatively large range—from x_0 to π—during the particle's evolution. Therefore, a simple Taylor expansion is insufficient to eliminate the nonlinearity in x. However, drawing inspiration from the work of Nath *et al.* [24], who demonstrated that the dynamical richness observed in the TG vortex flow can also be captured using a synthetic flow composed of piecewise linear functions, we can adopt a similar

strategy here. In their study, the sine function was approximated using a triangular wave function, preserving the essential dynamical features of the system. Following this idea, we approximate the functions in the weakly nonlinear system (D1) by replacing $\sin x$ with $\mathrm{Trw}(x)$, and $\cos x$ with its derivative $\mathrm{Trw}'(x)$, where

$$\mathrm{Trw}(x) = \begin{cases} x & \text{if } x \in [0, \pi/2] \\ \pi - x & \text{if } x \in [\pi/2, \pi] \end{cases}, \quad \text{and} \quad \mathrm{Trw}'(x) = \begin{cases} 1 & \text{if } x \in [0, \pi/2] \\ -1 & \text{if } x \in (\pi/2, \pi] \end{cases}. \tag{D2}$$

Note that, for our purposes, the triangular wave approximation is only required in the interval $x \in [0, \pi]$, where the dynamics occur. However, in general, to ensure a consistent replacement for $\sin x$ and $\cos x$, the function must be extended over the entire domain. Specifically, the triangular wave function should be extended anti-periodically over the interval $x \in [\pi, 2\pi]$, and then continued periodically beyond, with an overall period of 2π to match the periodicity of the original sine function. After introducing these triangular wave approximations, we substitute them into the weakly nonlinear system (D1). This results in a simplification of the governing equations, which now reduce to a linear system of the form:

$$\left.\begin{aligned} \ddot{x} + \frac{R}{\mathrm{St}}\dot{x} - x\left(\frac{R}{\mathrm{St}} + 3(1-R)\right) = 0 \\ \ddot{y} + \frac{R}{\mathrm{St}}\dot{y} + y\left(\frac{R}{\mathrm{St}} - 3(1-R)\right) = 0 \end{aligned}\right\} \quad \text{if } x \in \left[0, \frac{\pi}{2}\right], \tag{D3}$$

and

$$\left.\begin{aligned} \ddot{x} + \frac{R}{\mathrm{St}}\dot{x} + x\left(\frac{R}{\mathrm{St}} - 3(1-R)\right) = \pi\left(\frac{R}{\mathrm{St}} - 3(1-R)\right) \\ \ddot{y} + \frac{R}{\mathrm{St}}\dot{y} - y\left(\frac{R}{\mathrm{St}} + 3(1-R)\right) = 0 \end{aligned}\right\} \quad \text{if } x \in \left[\frac{\pi}{2}, \pi\right]. \tag{D4}$$

We first solve the governing equations from Eq. (D3) with the initial conditions: $x(t=0) = x_0$, $\dot{x}(t=0) = 0$, $y(t=0) = 0$, $\dot{y}(t=0) = v_{y_0}$, up to a time $t_{1/2}$ such that $x(t = t_{1/2}) = \pi/2$. The corresponding solution is given by

$$x(t) = x_0 \exp\left(-\frac{R\,t}{2\,\mathrm{St}}\right)\left\{\cosh\left(\frac{\alpha\,t}{2\,\mathrm{St}}\right) + \frac{R}{\alpha}\sinh\left(\frac{\alpha\,t}{2\,\mathrm{St}}\right)\right\}, \tag{D5a}$$

$$y(t) = v_{y_0}\frac{2\,\mathrm{St}}{\beta}\exp\left(-\frac{R\,t}{2\,\mathrm{St}}\right)\sin\left(\frac{\beta\,t}{2\,\mathrm{St}}\right). \tag{D5b}$$

Here, $\alpha = \sqrt{R^2 + 4\,R\,\mathrm{St} + 12\,(1-R)\,\mathrm{St}^2}$, and $\beta = \sqrt{-R^2 + 4\,R\,\mathrm{St} - 12\,(1-R)\,\mathrm{St}^2}$, both of which are real-valued in region B. To determine the time $t_{1/2}$, we must solve for t such that $x(t) = \pi/2$, using the expression (D5a). However, solving this exactly is nontrivial. To proceed, we approximate the expression in Eq. (D5a) under the assumption $\alpha\,t_{1/2}/(2\,\mathrm{St}) \gg 1$, which allows the hyperbolic functions to be approximated as half of exponential as $\cosh(z) \approx \sinh(z) \approx \frac{1}{2}e^z$. Using this, the equation for $x(t)$ simplifies significantly, and we obtain the following reduced form to solve:

$$\frac{x_0}{2}\exp\left(-\frac{R\,t}{2\,\mathrm{St}}\right)\left\{\exp\left(\frac{\alpha\,t}{2\,\mathrm{St}}\right) + \frac{R}{\alpha}\exp\left(\frac{\alpha\,t}{2\,\mathrm{St}}\right)\right\} \approx \frac{\pi}{2}. \tag{D6}$$

The solution that gives the half-time as

$$t_{1/2} \approx \frac{2\,\mathrm{St}}{\alpha - R}\ln\left[\frac{\pi\,\alpha}{x_0\,(\alpha + R)}\right]. \tag{D7}$$

Using this expression for $t_{1/2}$, we can now evaluate the particle's position and velocity components at this time as

$$\dot{x}(t = t_{1/2}) \approx \frac{\pi\,(R + 3\,\mathrm{St}\,(1 - R))}{\alpha + R}, \tag{D8a}$$

$$y(t = t_{1/2}) \approx v_{y_0}\,\frac{2\,\mathrm{St}}{\beta}\left(\frac{x_0\,(\alpha + R)}{\pi\,\alpha}\right)^{R/(\alpha - R)} \sin\left(\frac{\beta}{(\alpha - R)}\,\ln\left[\frac{\pi\,\alpha}{x_0\,(\alpha + R)}\right]\right), \tag{D8b}$$

$$\dot{y}(t = t_{1/2}) \approx v_{y_0}\,\frac{\sqrt{R^2 + \beta^2}}{\beta}\left(\frac{x_0\,(\alpha + R)}{\pi\,\alpha}\right)^{R/(\alpha - R)} \cos\left(\frac{\beta}{(\alpha - R)}\,\ln\left[\frac{\pi\,\alpha}{x_0\,(\alpha + R)}\right] + \tan^{-1}\frac{R}{\beta}\right). \tag{D8c}$$

Along with these approximations, the value $x(t = t_{1/2}) = \pi/2$ can now serve as the initial conditions to determine the remaining portion of the trajectory segment by solving the governing equations (D4) over the interval $t \in [t_{1/2}, t_1]$, during which $x(t)$ evolves from $\pi/2$ to π. The corresponding solution is

$$x(t) = \pi - \frac{\pi}{2\,\beta}\sqrt{(2\,R - \alpha)^2 + \beta^2}\,\exp\left(-\frac{R\,t'}{2\,\mathrm{St}}\right)\cos\left(\frac{\beta\,t'}{2\,\mathrm{St}} - \tan^{-1}\left[\frac{2\,R - \alpha}{\beta}\right]\right), \tag{D9a}$$

$$\begin{aligned} y(t) = {} & 2\,\mathrm{St}\,v_{y_0}\left(\frac{x_0\,(\alpha + R)}{\pi\,\alpha}\right)^{R/(\alpha - R)} \exp\left(-\frac{R\,t'}{2\,\mathrm{St}}\right)\left\{\frac{1}{\alpha}\cos\left(\frac{\beta}{(\alpha - R)}\,\ln\left[\frac{\pi\,\alpha}{x_0\,(\alpha + R)}\right]\right)\right. \\ & \left.\times \sinh\left(\frac{\alpha\,t'}{2\,\mathrm{St}}\right) + \frac{1}{\beta}\sin\left(\frac{\beta}{(\alpha - R)}\,\ln\left[\frac{\pi\,\alpha}{x_0\,(\alpha + R)}\right]\right)\cosh\left(\frac{\alpha\,t'}{2\,\mathrm{St}}\right)\right\}, \end{aligned} \tag{D9b}$$

where $t' = t - t_{1/2}$. To determine the time at which this segment of the trajectory terminates, i.e., $t = t_1$, one can solve for $x(t) = \pi$ using Eq. (D9a), and obtain

$$t_1 = t_{1/2} + \frac{2\,\mathrm{St}}{\beta}\left\{\pi - \tan^{-1}\left[\frac{\beta}{2\,R - \alpha}\right]\right\}. \tag{D10}$$

Substituting this time into Eq. (D9b), we obtain $y(t = t_1) = y_1$ as

$$\begin{aligned} y_1 = {} & 2\,\mathrm{St}\,v_{y_0}\left(\frac{x_0\,(\alpha + R)}{\pi\,\alpha}\right)^{R/(\alpha - R)} \exp\left\{-\frac{R}{\beta}\left(\pi - \tan^{-1}\left[\frac{\beta}{2\,R - \alpha}\right]\right)\right\} \\ & \times\left[\frac{1}{\alpha}\cos\left(\frac{\beta}{(\alpha - R)}\,\ln\left[\frac{\pi\,\alpha}{x_0\,(\alpha + R)}\right]\right)\sinh\left\{\frac{\alpha}{\beta}\left(\pi - \tan^{-1}\left[\frac{\beta}{2\,R - \alpha}\right]\right)\right\}\right. \\ & \left.+\frac{1}{\beta}\sin\left(\frac{\beta}{(\alpha - R)}\,\ln\left[\frac{\pi\,\alpha}{x_0\,(\alpha + R)}\right]\right)\cosh\left\{\frac{\alpha}{\beta}\left(\pi - \tan^{-1}\left[\frac{\beta}{2\,R - \alpha}\right]\right)\right\}\right]. \end{aligned} \tag{D11}$$

Note that this is an approximate expression, owing to the various approximations and linearizations employed in reaching here. Now, to determine the condition under which $|y_1|$ becomes smaller than x_0 (which, without loss of generality, we have taken as positive), we evaluate the ratio $|y_1|/x_0$. We find that this ratio depends on the initial conditions as

$$\frac{|y_1|}{x_0} \propto |v_{y_0}|\,x_0^{(2\,R - \alpha)/(\alpha - R)}, \tag{D12}$$

where, not that there is an additional dependence on x_0, appearing within the sinusoidal functions—as evident from Eq. (D11), which is omitted here. Now, considering the asymptotic limit where $x_0 \ll 1$ (i.e., the particle starts very close to the CFP), for $|y_1|/x_0$ to decrease for any finite v_{y_0}, the necessary condition is that the exponent of x_0 must be positive; that is, $(2\,R - \alpha)/(\alpha - R) > 0$. Solving this yields the critical condition that $\mathrm{St} < \mathrm{St}_{c_q}$, the expression for St_{c_q} is given in Eq. (23).

The dependence of x_0 inside the sinusoidal terms, which is omitted here, does not affect the outcome since sine and cosine functions are bounded by unity. This implies that in region B, even if a particle escapes its initial vortex cell, as long as its $\mathrm{St} < \mathrm{St}_{c_q}$, it will eventually lose its kinetic energy while traversing near CFPs, and numerically, it will end up getting captured by one—thus classified under region IIIa. However, if $\mathrm{St} > \mathrm{St}_{c_q}$, then the particle can gain kinetic energy, resulting in unbounded motion (classified as region II). The critical curve corresponding to St_{c_q} is shown in Fig. 10(a) as a yellow, dash-dotted line. This curve aligns quite well with the numerically identified boundary separating regions II and IIIa. For $R = 1$, the critical value we got here is $\mathrm{St}_{c_q} = 0.75$, which closely matches the previously reported value of 0.77 by Nath *et al.* [24]. However, the actual boundary is rather irregular, and the deviation may be attributed to: (i) the linearizations and approximations involved in our derivation here, and (ii) as discussed in the main text, near this boundary, particles can also become trapped in closed, periodic limit-cycle trajectories, depending on the choice of parameters and initial conditions—in addition to getting captured by CFPs. These limit cycles have not been incorporated into our present model. We anticipate that including them could yield a more accurate prediction of the boundary than what is obtained in this Appendix.

APPENDIX E: ROLE OF HISTORY FORCE ON PARTICLE LEAKAGE FROM VORTEX CELLS AND THEIR LONGTIME BALLISTIC DYNAMICS

We have shown in Secs. III C and V that in the presence of a history force, particles cross the separatrix line regardless of parametric and initial conditions and exhibit longtime ballistic dynamics. In this Appendix, we analyze the contribution of the history force close to the stagnation zones and separatrices to understand the underlying mechanism behind this crossing. We write the reduced order particle velocity as the summation of flow velocity and correction terms due to the particle inertia, added mass, and history effects, which appear in terms of fluid acceleration using the approach of Ferry and Balachandar [15]. The reduced order particle velocity in the limit $\mathrm{St} \ll R$ reads as follows:

$$\frac{dx}{dt} = \sin x \cos y - \mathrm{St}\left(\frac{3R-2}{2R}\right)\sin 2x + \mathrm{St}^{3/2}\frac{\kappa}{\sqrt{\pi}}\left(\frac{3R-2}{R}\right)F_x, \tag{E1a}$$

$$\frac{dy}{dt} = -\sin y \cos x - \mathrm{St}\left(\frac{3R-2}{2R}\right)\sin 2y + \mathrm{St}^{3/2}\frac{\kappa}{\sqrt{\pi}}\left(\frac{3R-2}{R}\right)F_y, \tag{E1b}$$

where

$$F_x = \int_{-\infty}^{t} \frac{dt'}{\sqrt{t-t'}} \sin x' \cos y' \cos 2x', \tag{E2a}$$

$$F_y = -\int_{-\infty}^{t} \frac{dt'}{\sqrt{t-t'}} \sin y' \cos x' \cos 2y' \tag{E2b}$$

are the contribution from the history force. Following the approach of Druzhinin and Ostrovsky [30], we consider the particle motion in the vicinity of a horizontal separatrix (see trajectory segment AB in Fig. 18), say $y \simeq \epsilon_y$ and $0 \lesssim x \lesssim \pi$. To the leading order, the particle motion is described by the following equation:

$$\frac{dx}{dt} = \sin x, \tag{E3}$$

where ϵ_y is a vanishingly small positive quantity. We integrate the Eq. (E3) with initial condition $x(t \to -\infty) = 0$ to get the particle trajectory of the following form:

$$x(t) = 2\,\tan^{-1}(e^t). \tag{E4}$$

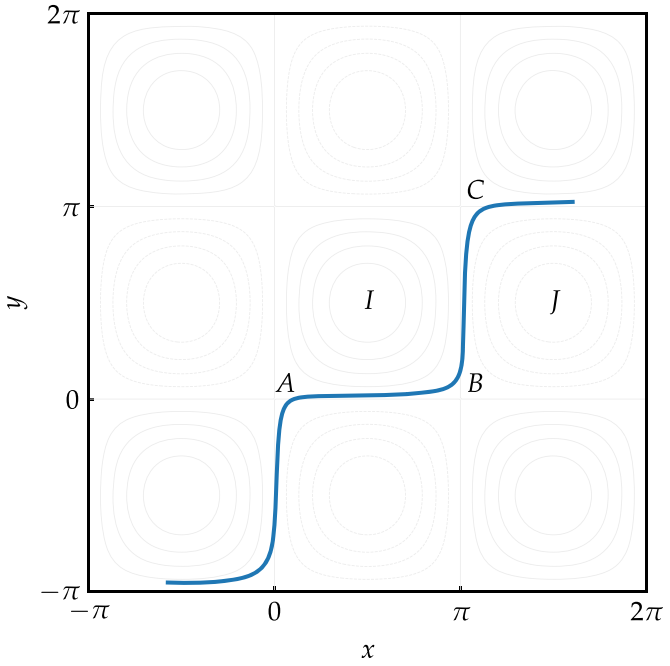

FIG. 18. Typical particle trajectory in the presence of the history force. Points A, B, and C mark locations where the trajectory crosses the separatrix, each situated near a stagnation point.

The solution gives the asymptotic condition $x(t \to \infty) = \pi$. Thus, a particle that starts near the stagnation point (0,0) travels close to the horizontal separatrix and, in the longtime limit, reaches the stagnation point at $(0, \pi)$. We now evaluate the contribution of history integrals in Eq. (E2) along the leading order trajectory defined by Eqs. (E4) as

$$F_x \approx \int_{-\infty}^{t} \frac{dt'}{\sqrt{t-t'}} \sin x' \cos 2x' = \int_{-\infty}^{t} \frac{dt'}{\sqrt{t-t'}} \sin\left(2\tan^{-1}(e^{t'})\right) \cos\left(4\tan^{-1}(e^{t'})\right), \quad \text{(E5a)}$$

$$F_y \approx -\epsilon_y \int_{-\infty}^{t} \frac{dt'}{\sqrt{t-t'}} \cos x' = -\epsilon_y \int_{-\infty}^{t} \frac{dt'}{\sqrt{t-t'}} \cos\left(2\tan^{-1}(e^{t'})\right). \quad \text{(E5b)}$$

In the limit $t \to \infty$, as the particle approaches near stagnation point at $(0, \pi)$, F_x approaches a positive value and F_y approaches a very large negative value (for positive ϵ_y), which acts on the particles to push them out of the cell I. Now we consider the trajectory segment BC, close to the vertical separatrix line associated with the next cell J with $x \simeq \pi + \epsilon_x$ and $0 \lesssim y \lesssim \pi$, where the equations of particle motion at the leading order are the following:

$$\frac{dy}{dt} = \sin y. \quad \text{(E6)}$$

We integrate the Eq. (E6) with the initial condition $y(t \to -\infty) = 0$ to get the particle trajectory of the following form as early as

$$y(t) = 2\tan^{-1}(e^{t}). \quad \text{(E7)}$$

Here as well, in the longtime limit, $y(t \to \infty) = \pi$, meaning the particle moves from near the stagnation point at $(\pi, 0)$ toward the vicinity of the stagnation point at (π, π), close to the vertical

separatrix, taking an infinite amount of time to reach it. As earlier, we now evaluate the history force along this segment of the trajectory, defined by Eq. (E7), using Eqs. (E2) as

$$F_x \approx \int_{-\infty}^{t} \frac{dt'}{\sqrt{t-t'}} \sin x' \cos y' = -\epsilon_x \int_{-\infty}^{t} \frac{dt'}{\sqrt{t-t'}} \cos\left(2\tan^{-1}(e^{t'})\right), \tag{E8a}$$

$$F_y \approx \int_{-\infty}^{t} \frac{dt'}{\sqrt{t-t'}} \sin y' \cos 2y' = \int_{-\infty}^{t} \frac{dt'}{\sqrt{t-t'}} \sin\left(2\tan^{-1}(e^{t'})\right) \cos\left(4\tan^{-1}(e^{t'})\right). \tag{E8b}$$

Here, in the limit $t \to \infty$, the force component F_x becomes a very large negative value (for positive ϵ_x), while F_y approaches a positive value. Here also both components act to push the particle out of the vortex cell J, thereby facilitating cross-cell transport. This supports the earlier observation by Druzhinin and Ostrovsky [30] that the history force can cause heavy particles with nonzero inertia to leak out of vortex cells without requiring a critical Stokes number threshold. In addition, our analysis demonstrates that the history force near the fixed points is nonzero and contributes significantly to displacing the particle out of the cell. Interestingly, along both trajectory segments, the components of the history force alternate in sign. This alternating behavior leads to a zigzag-like motion of the particles close to the separatrix lines as shown in Fig. 18. Over time, this repeated zigzag motion results in a directed motion on average, ultimately causing the particle dynamics to become ballistic at long times.

[1] C. Kleinstreuer and Z. Zhang, Airflow and particle transport in the human respiratory system, Annu. Rev. Fluid Mech. **42**, 301 (2010).

[2] J. M. Martel and M. Toner, Inertial focusing in microfluidics, Annu. Rev. Biomed. Eng. **16**, 371 (2014).

[3] G. Falkovich, A. Fouxon, and M. Stepanov, Acceleration of rain initiation by cloud turbulence, Nature (London) **419**, 151 (2002).

[4] T. Sapsis and G. Haller, Inertial particle dynamics in a hurricane, J. Atmos. Sci. **66**, 2481 (2009).

[5] E. E. Michaelides, M. Sommerfeld, and B. van Wachem, *Multiphase Flows with Droplets and Particles* (CRC Press, Boca Raton, FL, 2022).

[6] M. R. Maxey and J. J. Riley, Equation of motion for a small rigid sphere in a nonuniform flow, Phys. Fluids **26**, 883 (1983).

[7] M. Maxey, The motion of small spherical particles in a cellular flow field, Phys. Fluids **30**, 1915 (1987).

[8] J. Bec, K. Gustavsson, and B. Mehlig, Statistical models for the dynamics of heavy particles in turbulence, Annu. Rev. Fluid Mech. **56**, 189 (2024).

[9] A. Daitche, Advection of inertial particles in the presence of the history force: Higher order numerical schemes, J. Comput. Phys. **254**, 93 (2013).

[10] S. G. Prasath, V. Vasan, and R. Govindarajan, Accurate solution method for the Maxey–Riley equation, and the effects of basset history, J. Fluid Mech. **868**, 428 (2019).

[11] M. Wilkinson and B. Mehlig, Caustics in turbulent aerosols, Europhys. Lett. **71**, 186 (2005).

[12] J. Bec, Fractal clustering of inertial particles in random flows, Phys. Fluids **15**, L81 (2003).

[13] J. Bec, A. Celani, M. Cencini, and S. Musacchio, Clustering and collisions of heavy particles in random smooth flows, Phys. Fluids **17**, 073301 (2005).

[14] M. Maxey, Simulation methods for particulate flows and concentrated suspensions, Annu. Rev. Fluid Mech. **49**, 171 (2017).

[15] J. Ferry and S. Balachandar, A fast Eulerian method for disperse two-phase flow, Int. J. Multiphase Flow **27**, 1199 (2001).

[16] M. R. Maxey, The gravitational settling of aerosol particles in homogeneous turbulence and random flow fields, J. Fluid Mech. **174**, 441 (1987).

[17] O. Druzhinin, On the two-way interaction in two-dimensional particle-laden flows: The accumulation of particles and flow modification, J. Fluid Mech. **297**, 49 (1995).

[18] G. Haller and T. Sapsis, Where do inertial particles go in fluid flows? Physica D **237**, 573 (2008).
[19] A. Crisanti, M. Falcioni, A. Provenzale, and A. Vulpiani, Passive advection of particles denser than the surrounding fluid, Phys. Lett. A **150**, 79 (1990).
[20] A. Crisanti, M. Falcioni, A. Provenzale, P. Tanga, and A. Vulpiani, Dynamics of passively advected impurities in simple two-dimensional flow models, Phys. Fluids **4**, 1805 (1992).
[21] L.-P. Wang, M. Maxey, T. Burton, and D. Stock, Chaotic dynamics of particle dispersion in fluids, Phys. Fluids **4**, 1789 (1992).
[22] N. Raju and E. Meiburg, Dynamics of small, spherical particles in vortical and stagnation point flow fields, Phys. Fluids **9**, 299 (1997).
[23] A. V. S. Nath, A. Roy, R. Govindarajan, and S. Ravichandran, Transport of condensing droplets in Taylor-Green vortex flow in the presence of thermal noise, Phys. Rev. E **105**, 035101 (2022).
[24] A. V. S. Nath, A. Roy, S. Ravichandran, and R. Govindarajan, Irregular dependence on Stokes number, and nonergodic transport, of heavy inertial particles in steady laminar flows, Phys. Rev. Fluids **9**, 014302 (2024).
[25] G. I. Taylor, *Notes on Possible Equipment and Technique for Experiments on Icing on Aircraft* (Her Majesty's Stationery Office, London, UK, 1940).
[26] R. Klages, Sol Selene Gil Gallegos, J. Solanpää, M. Sarvilahti, and E. Räsänen, Normal and anomalous diffusion in soft Lorentz gases, Phys. Rev. Lett. **122**, 064102 (2019).
[27] A. V. Nath and A. Roy, Clustering and chaotic motion of heavy inertial particles in an isolated nonaxisymmetric vortex, J. Fluid Mech. **998**, A62 (2024).
[28] Y. Dagan, Analytical solutions for particle dispersion in Taylor–Green vortex flows, Theor. Comput. Fluid Dyn. **39**, 14 (2025).
[29] J. C. Lasheras and K.-K. Tio, Dynamics of a small spherical particle in steady two-dimensional vortex flows, Appl. Mech. Rev. **47**, S61 (1994).
[30] O. Druzhinin and L. Ostrovsky, The influence of Basset force on particle dynamics in two-dimensional flows, Physica D **76**, 34 (1994).
[31] F. Candelier, J. Angilella, and M. Souhar, On the effect of the Boussinesq–Basset force on the radial migration of a Stokes particle in a vortex, Phys. Fluids **16**, 1765 (2004).
[32] A. Daitche, On the role of the history force for inertial particles in turbulence, J. Fluid Mech. **782**, 567 (2015).
[33] D. Jaganathan, S. G. Prasath, R. Govindarajan, and V. Vasan, The Basset–Boussinesq history force: Its neglect, validity, and recent numerical developments, Front. Phys. **11**, 1167338 (2023).
[34] S. Balachandar, *Fundamentals of Dispersed Multiphase Flows* (Cambridge University Press, Cambridge, UK, 2024).
[35] I. Langmuir and K. Blodgett, A Mathematical Investigation of Water Droplet Trajectories, Technical Report No. 5418 (Army Air Forces Headquarters, Air Technical Service Command, Washington, DC, 1946).
[36] L. Hofmann, B. Rieck, and F. Sadlo, Visualization of 4D vector field topology, in *Computer Graphics Forum* (Wiley Online Library, 2018), Vol. 37, pp. 301–313.
[37] D. Ingham, L. Hildyard, and M. Hildyard, On the critical Stokes' number for particle transport in potential and viscous flows near bluff bodies, J. Aerosol Sci. **21**, 935 (1990).
[38] L. M. Levin, Deposition of particles from a flow of aerosol onto obstacles, Dokl. Akad. Nauk SSSR **91**, 1329 (1953).
[39] A. G. Konstandopoulos, M. J. Labowsky, and D. E. Rosner, Inertial deposition of particles from potential flows past cylinder arrays, J. Aerosol Sci. **24**, 471 (1993).
[40] D. Lesnic, L. Elliott, and D. B. Ingham, On Levin's theorem for the critical stokes number, J. Aerosol Sci. **24**, S151 (1993).
[41] M. Massot, Eulerian multi-fluid models for polydisperse evaporating sprays, *Multiphase Reacting Flows: Modeling and Simulation* (Springer, Berlin, 2007), pp. 79–123.
[42] S. Bosi and D. Desmarchelier, Local bifurcations of three and four-dimensional systems: A tractable characterization with economic applications, Math. Soc. Sci. **97**, 38 (2019).

[43] M. A. Zaks, A. S. Pikovsky, and J. Kurths, Steady viscous flow with fractal power spectrum, Phys. Rev. Lett. **77**, 4338 (1996).
[44] M. A. Zaks and A. V. Straube, Steady Stokes flow with long-range correlations, fractal Fourier spectrum, and anomalous transport, Phys. Rev. Lett. **89**, 244101 (2002).
[45] M. A. Zaks and A. Nepomnyashchy, Subdiffusive and superdiffusive transport in plane steady viscous flows, Proc. Natl. Acad. Sci. USA **116**, 18245 (2019).
[46] P. Alexander, High order computation of the history term in the equation of motion for a spherical particle in a fluid, J. Sci. Comput. **21**, 129 (2004).
[47] M.A.T. van Hinsberg, J. ten Thije Boonkkamp, and H. J. Clercx, An efficient, second order method for the approximation of the Basset history force, J. Comput. Phys. **230**, 1465 (2011).
[48] H. A. Elghannay and D. K. Tafti, Development and validation of a reduced order history force model, Int. J. Multiphase Flow **85**, 284 (2016).
[49] D. Jaganathan, R. Govindarajan, and V. Vasan, Explicit Runge-Kutta algorithm to solve nonlocal equations with memory effects: Case of the Maxey-Riley-Gatignol equation, Quart. Appl. Math. **83**, 135 (2025).
[50] P. M. Lovalenti and J. F. Brady, The hydrodynamic force on a rigid particle undergoing arbitrary time-dependent motion at small Reynolds number, J. Fluid Mech. **256**, 561 (1993).
[51] R. Mei, Flow due to an oscillating sphere and an expression for unsteady drag on the sphere at finite Reynolds number, J. Fluid Mech. **270**, 133 (1994).
[52] A. Dorgan and E. Loth, Efficient calculation of the history force at finite Reynolds numbers, Int. J. Multiphase Flow **33**, 833 (2007).
[53] P. Kumar, P. Jutur, A. Roy, and M. Panchagnula, Stirring with the phase angle ϕ: Unlocking chaos in slow subperiodic viscous flows, Phys. Rev. Fluids **10**, 064101 (2025).